HABIBU AMINU HUSSAIN

IZMIR KATIP CELEBI UNIVERSITY

2021

IZMIR KATIP CELEBI UNIVERSITY

GRADUATE SCHOOL OF NATURAL AND APPLIED SCIENCES

A FIRST PRINCIPLE INVESTIGATION OF THE EFFECT OF VACANCIES ON STRUCTURAL, ELECTRONIC AND MAGNETIC PROPERTIES OF GRAPHENE hBN (HEXAGONAL-BORON NITRIDE) IN-PLANE HYBRID

PhD THESIS

HABIBU AMINU HUSSAIN

Department of Nanotechnology

FEBRUARY 2021

Habibu Aminu HUSSAIN, PhD student of **IKCU Graduate School of Natural and Applied Sciences,** successfully defended the thesis entitled **"A FIRST PRINCIPLE INVESTIGATION OF THE EFFECT OF VACANCIES ON STRUCTURAL, ELECTRONIC AND MAGNETIC PROPERTIES OF GRAPHENE HEXAGONAL-BORON NITRIDE IN-PLANE HYBRID",** which he prepared after fulfilling the requirements specified in the associated legislations, before the jury whose signatures are below.

Thesis Advisor :

Prof. Dr. Cem ÖZDOĞAN .....
İzmir Katip Çelebi Üniversitesi

Jury Members :

Prof. Dr. Nurten AKMAN …….
Mersin Üniversitesi

Doç.Dr. Serkan ATEŞ .....
İzmir Yukşek Teknoloji Enstitüsü (İYTE)

Doç.Dr. Mustafa EROL .....
Dokuz Eylül Üniversitesi

Dr. Öğr. Üyesi Ahmet AYKAÇ …….
İzmir Katip Çelebi Üniversitesi

Date of Submission : 18.01.2021
Date of Defense : 15.02.2021

FOREWORD

Above all, I would like to appreciate, profoundly my supervisor Prof. Dr. Cem ÖZDOĞAN who had supported me always. He provided excellent suggestion and feedback on my thesis, with constructively pointing out my mistakes. Without his guidance, I cannot grow so fast in my research. Profound appreciation goes to my co-supervisor Prof. Dr. Nurten AKMAN who contributed immensely throughtout my research work. To the jury members too that give their time during this period Assoc. Prof. Dr. Serkan ATEŞ and Assoc. Prof. Dr. Mustafa EROL.

Special thanks go to my brother Munir Aminu for his great assistance and understanding. I must appreciate my friends, brothers and sisters for the wonderful support I received from them throughout my entire studies.

I would also like to appreciate the entire academic and administrative staff of Izmir Katip Celebi University , particularly the Graduate School of Natural and Applied Sciences. The library and computer facilities of the University have been very helpful. Propound gratitude also goes to the Department of Nanotechnology staffs for their assistance throughout my PhD studies, particularly the head of department, Prof. Dr. Şerafettin Demiç

Last but not the least; I would like to show my appreciation my entire family. First, my parents Haj. Maryam Muhammad Dankadai and Alhj. Aminu Hussain for supporting me spiritually throughout my life.

This thesis was supported by Izmir Katip Celebi University, Coordination Office of Scientific Research Projects…

FEBRUARY 2021 Habibu Aminu Hussain

TABLE OF CONTENTS

ABBREVIATIONS

CG → Conjugated gradient

DOS → Density of States

CVD → Chemical Vapor Deposition

DFT → Density Functional Theory

G → Graphene

GBN → Graphene/Hexagonal Boron Nitride

h-BN → hexagonal boron nitride

GGA → Generalized Gradient Approximation

LDA → Local density approximation

VASP → Vienna Ab Initio Simulation Package

PAW → Projected Augmented Wave

LIST OF TABLES

Page

LIST OF FIGURES

Page

A FIRST PRINCIPLE INVESTIGATION OF THE EFFECT OF VACANCIES ON STRUCTURAL, ELECTRONIC AND MAGNETIC PROPERTIES OF GRAPHENE hBN (HEXAGONAL-BORON NITRIDE) IN-PLANE HYBRID

ABSTRACT

Producing a thin sheet of graphene/hexagonal boron nitride (GBN) hybrid without defect for practical applications is nearly impossible. In this research, a detailed discussion was made on two distinct types of nanosheet structures. First, a hexagonal boron nitride (h-BN) nanosheet (layout) hosts a diamond shaped graphene (G) island (XG@hBN). Second, a graphene nanosheet (layout) hosts a diamond shaped h-BN island (Xh-BN@G). X represents the size of diamond shaped island and its value is 4, 9 and 16. X is also the number of hexagonal units in diamond shaped island. A single vacancy was created by removing a nitrogen (N), carbon (C), or boron (B) atom in GBN nanosheet. The stabilities, magnetic and electronic properties of defect-free and vacancy defected GBN hybrids were analyzed by using the density functional theory (DFT) in detail. For the case of XG@h-BN nanosheets involving graphene islands with size X, the formation energies of VB_L and VC_{I2} decrease with enlarging G island. However, the formation energy of VC_{1I} does not vary with the size of G island (X). The magnetization energy (ΔE_M) of hybrid with VC_i defect is negative as the size of G island (X) is 9. Our research found that the ΔE_M of other defective hybrids have positive values. The VC in hybrids with defect were discovered to possess no magnetic moment except for 16G(D-VC_{I2})@h-BN. The VC_{I1} in hybrids with defect show very small magnetization energy and non-magnetic properties. As the G island is in size 16, the VC_{I2} defected hybrid has a total magnetic moment of 2 μB, and a magnetization energy of **115** meV. All VC_i defected hybrids do not possess magnetic moment. The C vacancy is the most energetically desirable defect for all sizes of G island. The VB_I defected nanosheet has a non-integer value of magnetic moment (0.4 μB) as the G island is in size 9. All defect-free (pure) hybrids do not acquire magnetic moment and therefore they are non-magnetic structures. The band gap of VN_L defected hybrid decreases with enlarging G island. As a result of this, we might expect a shift from semiconducting to metallic feature with further increase in G size. Moreover, the band gap of **VB_L** defected nanosheet expands the G island size increases. Defect-free hybrids including diamond shaped h-BN islands (Xh-BN@G) do not acquire magnetic moment and therefore they are non-

magnetic structures. The VC defects at the interface of hybrids were discovered to possess no magnetic moment except for the h-BN island with size 16. Likewise, all VN defected hybrids possess no magnetic moment except for the h-BN island in size 4. The VB_i defected nanosheets involving the h-BN islands in sizes 9 and 16 have the largest value of magnetization energies. Likewise, the **VB_L** defected hybrids involving the G islands in sizes of 9 and 16 have the highest amount of ΔE_M. The band gap of defect-free hybrid increases when the h-BN island increases. We could not obtain a correlation between the band gap of defective hybrid and the size of h-BN island embedded in G layout.

BOŞLUK KUSURLARININ GRAFEN/hBN (HEGZAGONAL BOR NİTRÜR) DÜZLEM İÇİ HİBRİTİNİN YAPISAL, ELEKTRONİK VE MANYETİK ÖZELLİKLERİNE ETKİSİNİN İLK İLKELER YÖNTEMİ İLE ARAŞTIRILMASI

ÖZET

Pratik kullanım amaçlı üretim sırasında kusur oluşturmadan ince bir grafen/altıgen bor nitrür (GBN) hibrit yaprağı üretmek neredeyse imkansızdır. Bu araştırmada, iki farklı yapı türü hakkında ayrıntılı bir tartışma yapılmıştır. İlk olarak, elmas şeklinde bir grafen (G) adası barındıran altıgen bor nitrür (h-BN) nano yaprak (XG @ h-BN) analiz edildi. İkinci olarak, elmas şekilli bir h-BN adası barındıran grafen nano yaprak (Xh-BN @ G) incelenmiştir. X, elmas şekilli adacığın boyutunu göstermekte olup 4, 9 ve 16 değerlerini almaktadır. Elmas şekle sahip olan bir adacıkta en küçük hücre altıgen biçimde olup bu hücre sayılarının toplamı X e karşı gelmektedir. Boşluk kusuru, GBN nano yapraktan bir N, C veya B atomu kopartılarak oluşturulmuştur. Kusursuz ve buşluk kusurlu GBN hibritinin kararlılığı, elektronik ve manyetik özellikleri yoğunluk fonksiyonel teori (DFT) kullanılarak kapsamlı bir şekilde analiz edildi. XG @ h-BN olarak gösterilen X boyutlu grafen adacıklı hibritlerde, G ada boyutunun (X) artmasıyla VB_L ve VC_{I2}' nin boşluk oluşum enerjisi azalmaktadır. Bununla birlikte, VC_{I1}' nin oluşum enerjisi, grafen ada boyutundaki (X) değişimle değişmez. G ada boyutu 9 olan VC_i boşluklu hibritte manyetik enerjinin negatif olduğu gözlemlendi. Araştırmalarımıza göre diğer tüm kusurlu hibritlerin manyetik enerjileri pozitif değerli bulunmuştur. VC kusurlu hibritlerin, 16G (D-VC_{I2}) @ h-BN hariç, manyetik momente sahip olmadığı keşfedildi. VC_{I1} boşluklu hibritlerin tamamı çok küçük manyetik enerjiye sahip olup manyetik olmayan özellik gösterirler. Boyutu 16 olan G adası için, VC_{I2} boşluklu hibrid 2 μB toplam manyetik momente ve **115** meV manyetik enerjiye sahiptir. VC_i boşluklu hibritlerin tamamının manyetik momenti yoktur. C boşluğu, G adasının her boyutu için, enerjik olarak en çok arzu edilen kusurdur. G ada boyutu 9 olan VB_I kusurlu nano-yaprak tamsayı olmayan manyetik momente (0.4 μB) sahiptir. Ayrıca, G ada boyutu arttıkça bu hibritin manyetik momenti 1 μB'ye yükselir. Kusursuz (saf) hibritlerin tamamının manyetik momenti yoktur ve bu nedenle manyetik olmayan yapılardır. VN_L boşluklu hibritlerin enerji bant aralığı, büyüyen G adasıyla azalmaktadır. Bunun sonucu olarak, G ada boyutunun daha da artmasıyla yarı iletkenden metalik özelliğe geçiş yapabileceğimiz tahmin edilebilir. Dahası, **VB_L** kusurlu nanosheet' in enerji

bant aralığı, artan ada boyutu ile genişler. Elmas şekilli h-BN adacığa sahip kusursuz hibritlerin (Xh-BN @ G) manyetik momenti yoktur ve bu nedenle manyetik olmayan yapılardır. Arayüzeyde VC kusuru olan hibritlerin, h-BN boyutu 16 olan hariç, manyetik moment içermediği keşfedildi. Benzer şekilde, VN kusurlu hibritlerin tamamı, h-BN adasının boyutu 4 olan hariç, manyetik momente sahip değildir. H-BN boyutu 9 ve 16 olan VB_i boşluklu nano yapraklar en büyük manyetik enerjiye (ΔE_M) sahiptir. Benzer şekilde, G ada boyutu 9 ve 16 olan **VB_L** kusurlu hibritler en yüksek manyetik enerjiye (ΔE_M) sahiptir. Kusursuz hibritlerin bant aralığı, artan h-BN ada boyutuyla artmaktadır. Kusurlu hibritin bant aralığı ile grafene eklenmiş h-BN ada boyutu arasında bir korelasyon (ilişki) elde etmedik.

1.0 INTRODUCTION

The extraction of single-atom-thick graphene from bulk graphite in 2004 [1] has led to the massive interest in other single layer materials with or without honeycomb structure by the scientific community. One of the stable one similar to graphene is the boron nitride in hexagonal form (h-BN). The ideal lattice match between h-BN and graphene make it possible to create graphene/h-BN in-plane hybrids (GBN) structure. The honeycomb lattice of carbon atoms makes it an attractive structure in fundamental physics and some other electronic devices, such as capacitors and field effect transistors [2, 3]. Moreover, tuning its band gap might further increase its application in optoelectronic and nanoelectronics devices. Various methods have been proposed to open an energy gap between the conduction and valence band. Chemical modifications, including chemically doping graphene with imported atoms are among the strategies.[4]. The properties of purest graphene are outstanding. Being the one of the hardest material so far to be tested, the effectiveness, conduction of heat and electricity and almost transparent make graphene one of the favorable materials for researchers in nanotechnology [5].

Structural defect in graphene is inevitable during the growth or processing. External atoms could intentionally be introduced into graphene as impurities forming extrinsic defect that alter the type and amount of charge defect in the system. Nitrogen and boron are desirable dopants in graphene nanostructures because they just possess one electron more or less to that of carbon [6, 7]. The presence of single vacancy has fascinating and unanticipated implication. It leads to the emergence of a stable unit charge stationed around the vacancy site and interfering through conduction with other charges through an unscreened coulomb potential [8, 9].

My thesis research focuses on exploring the energetics of both defective h-BN domain in graphene sheets and graphene domain in h-BN sheet by using DFT computations. The analysis of the electronic band structure of the GBN hybrid with varied types of vacancies and sizes were conducted. The size of the island can alter the magnetic features and band gap of the hybrid system. The system has two sets of hybrid in terms of island formation: (i) a h-BN layout hosts a rhombic(diamond) shaped graphene island and (ii) a graphene layout hosts a diamond shaped h-BN island. The size of island (the number of hexagonal unit that the island involves) is 4, 9 or 16. The computational protocol focuses on creating a single-atom vacancy at various locations on a

GBN hybrid and also measuring the local DOSs at an atomic level. Mono vacancy alters the electronic properties of the hybrid. Magnetism arising from vacancy defect was also analyzed. The energetic of island implantation $\mathcal{E}_{if}$ (equation (2) and (3)) was determined for each island size. Vacancy formation energy E_{df} (equation (5)) for each vacancy was also determined. Magnetic energy ΔE_M (equation (1)) is the difference between the total energy of the SP and NSP calculations and it was also calculated in this thesis. The influences of these vacancies on magnetic, structural and electronic properties of the GBN hybrids were fully explored.

1.1 Graphene

The term "Graphene" was derived from "graphite" which is a crystal element of carbon and the suffix -ene, was named by a renowned German chemist Boehm in 1962[10]. Boehm is a professor at a university in Munich and he is considered by many people to be the leading figure in graphene research. The naming was first believed to emerge in the year 1987 [11] while trying to explain the creation of a mono layer of graphite from graphite intercalation compounds. When carbon atoms are arranged in a hexagonal form, the resulting product is a crystalline graphite. It forms naturally in this manner and under normal condition. Graphene is among the many allotropes of carbon and it is a mono layer of hexagonal arrangement of carbon atoms. Having a 2D structure, graphene is the only form of carbon that has all its atom accessible for chemical reaction from both sides. The C atoms in graphene creates a honeycomb mesh because of their sp^2 hybridization. Graphene has been produced in different ways and on various substrates. Within each layer of graphene, carbon atoms are glued to one another by powerful covalent bonds with a bond length of about 1.42 Å, while the inter layers are kept close by a non-strong van der Waal force [12]. The Mechanical separation of graphene from graphite was first realized in 2004[1].

The huge popularity that mechanical exfoliation method receives from researchers could be attributed to it being cheaper and simpler. However, the control of the shape and orientation of the grapheme layer are very difficult during the exfoliation of graphene. Epitaxial growth of graphene layer was reported during the annealing of hexagonal SiC crystal at high temperature [13]. Thermal decomposition was performed on the upper coating of SiC under normal annealing condition. During the thermal decomposition process, the Si atoms are ejected from the structure and the carbon atoms stay on the surface by repositioning themselves to form an epitaxial graphene layer

[14]. Graphene was also deposited on top of copper surface by chemical vapor deposition (CVD) method [15]. The solubility of carbon in copper is negligeable; therefore, graphene was created on Copper mainly by uninterrupted decomposition of the carbon carrying gas on the catalytic Copper layer.

The properties of purest graphene are outstanding. Being the toughest material ever tested, it conduct electricity and heat flawlessly and it is almost transparent [16]. Graphene is among the most favorable single layer materials for researchers in nanotechnology. But it is almost impossible to get rid of structural defect during its growth process. The defect which is often perceived as limiters, somehow found its own application in thermoelectric devices [17]. Graphene lattice can be reconstructed by creating non-hexagonal rings, [18] which does not involve missing or additional atoms. It is demonstrated that by turning the C-C bond by 90°, hexagons can be converted into a couple of heptagons and pentagons. This is known as the Stone-Wales defect and it was proved to exist in the graphene layer previously [19]. Impurities that alter the type of charge defect in the graphene can be introduced into the graphene, as well. Due to their fascinating electronic properties, graphene and other low dimensional honeycomb structures such as carbon nanotubes and fullerenes have found huge applications in nanoelectronics [20]. For example the potential use of graphene in the field effect transistor and semiconductor electronics was explored by simply tuning its band gap [20]. It's much more easier to grow a well align graphene layer on top of h-BN substrate [21, 22], than to grow an in-plane graphene in h-BN substrate [23]. This is due to the fact that producing such an in-plane structure with lack of defect is quite difficult during the production processes.

Chemical modification of the graphene through external atoms is one of the well-known techniques to open an energy gap in the graphene [24, 25]. Hydrogenation [26], exerting an electric force [26] or decreasing its dimension [27] are also alternative approaches to open an energy gap in the graphene. Multiple vacancy and Stone Wales (SW) defect could lead to band gap opening in the graphene [28]. **Figure 1** shows the optimized geometry of a graphene unit cell (a) and its electronic band structure (b). As expected, graphene is a semimetal at Γ point.

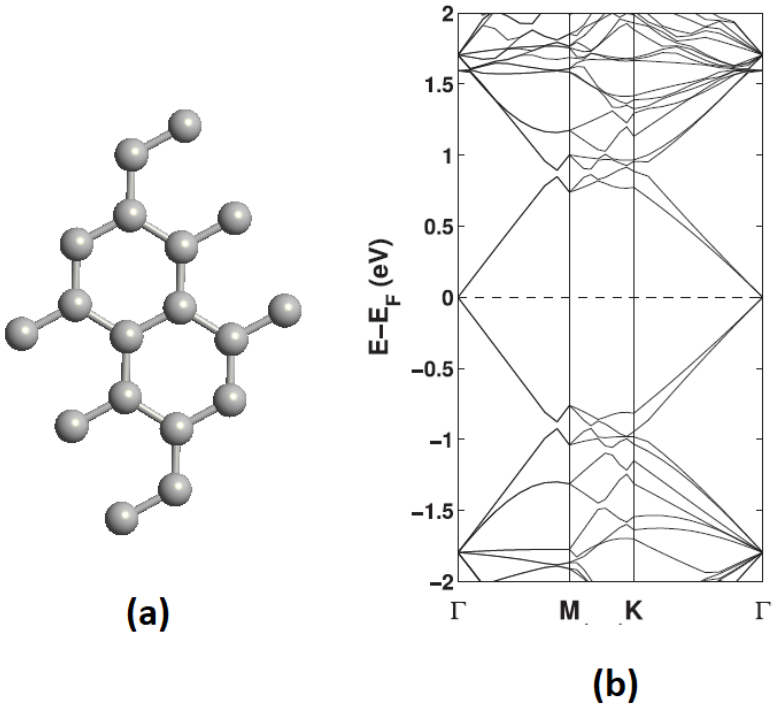

Figure 1 (a) Optimized geometry of graphene unit cell with two atoms. The bond length is about 1.42 Å. (b) Electronic band structure of graphene. Graphene is a semimetal at Γ point.

1.2 Hexagonal Boron Nitride

Hexagonal boron nitride (h-BN) is a graphite like layered material, and it consists of alternating boron (B) and nitrogen (N) atoms in a honeycomb arrangement. The N and B atoms are interchangeably arranged to create a conjugated planer layer. The layers bound together to make the immediate atomic layer on top of one another due to a polarity mismatch [20, 30]. A powerful covalent bond ties the nitrogen and boron atoms together to create a h-BN layer [30]. Polarity mismatch arises when a negatively charge nitrogen atom is placed above the positively charge boron atom. The application of h-BN was dated back to as early as 1940 when it was used to make cosmetics in Japan. Challenges and difficulty in manufacturing forces this application to be abandoned. The comeback for relatively mass production of h-BN starts from early 1900s when the production and optimization processes get a boost from improve production process. The cosmetic industry jumps once again and uses h-BN in various products like eye shadow, kohl pencil, lip sticks and many other [31]. Another application of h-BN is that it can be incorporated

in ceramics, plastics, alloys and many other materials, thanks to its chemical and external thermal stability that give it self-lubricating properties [31]. It is also used in electronics as an semiconductor substrate due to its good thermal and dielectric properties.

It is quite difficult to understand the nature and all the properties of high-quality h-BN because of the difficulties faced in synthesizing process. Providing an excellent quality h-BN for device application has always been a top challenge. For instance, it was recently proposed that h-BN could be an indirect band gap semiconductor [33, 34], while other recent researches demonstrate that h-BN could have a direct energy gap of about 5.90 eV [34]. The inconsistency might be ascribed to the use of low-quality h-BN film in the previous work. Under nonequilibrium conditions the early experimental proof of h-BN synthetization was revealed by Sokolowski [35]. Using chemical reaction, h-BN was produced synthetically by combining boric acid with ammonia in an enclosed nitrogen environment [36]. By employing centrifugation technique, Chunyi *et al.* experimentally produced several layers of h-BN and characterized the final structure using TEM and (SEM) [37] methods. Further research on the mechanical properties of multi layered defective h-BN was performed by Song [38]. They have discovered that when the number of defective site increases, the maximum stress decreases while maintaining a constant breaking strain. Optimized geometry of a h-BN unit cell and its band structure were presented in **Figure 2**.

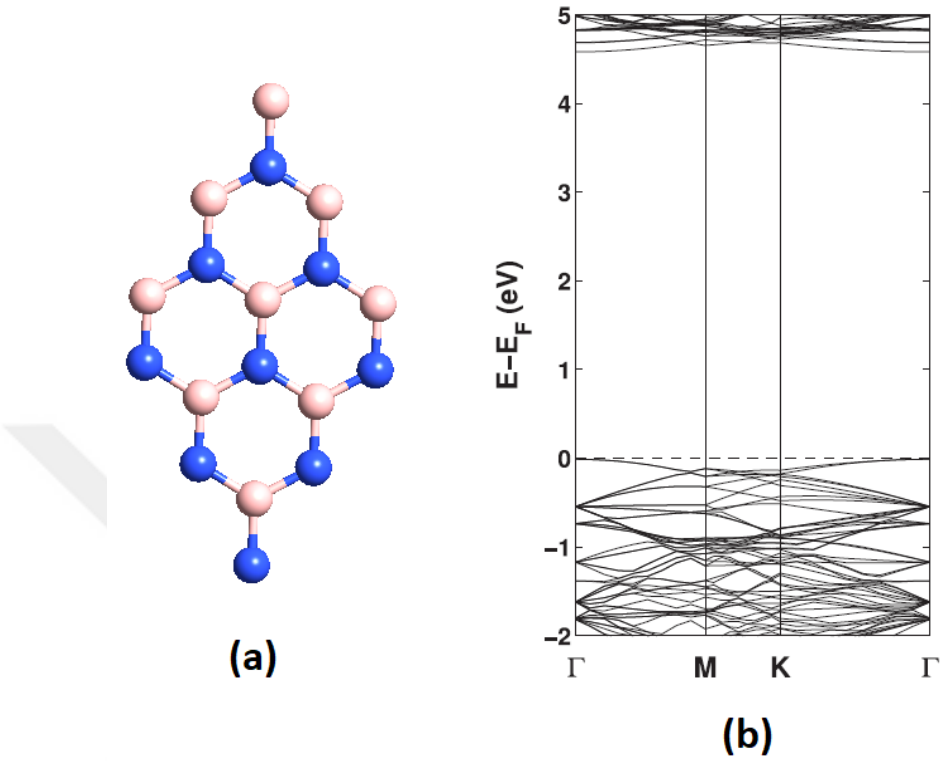

Figure 2 (a) Optimized geometry of hexagonal boron nitrogen unit cell with two atoms. The length of bond is about 1.45 Å. The pink spheres represent boron atoms while the blue ones represent nitrogen atoms. (b) Energy band structure of pristine h-BN having a wide band gap.

Many experimental and theoretical researches were conducted to explore the effects of defect on h-BN [40, 41]. For example, mechanical treatment was conducted using ball-mill on pristine micrometer h-BN sample containing tiny crystal particles to deliberately introduce defect into the h-BN [41]. Common defects observed in h-BN monolayer are the missing boron or nitrogen atoms. Vacancy type defects usually occur in h-BN during synthesis [43, 44]. Another type of defect found in h-BN is the replacement of either nitrogen or boron atom with carbon atom. This type of defect has its own implication. It was found that boron substitution with carbon in a medium full of N atoms or nitrogen substitution with carbon in a medium full of B atoms decreases the formation energies as compared to boron or nitrogen vacancy defect [41]

1.3 Graphene/Hexagonal Boron Nitride

Nano sheet comprising of B, C and N could result in a new material with excellent hybrid proper ties compared to h-BN and graphene. Theoretical studies foresaw the possibility of creating and characterizing GBN compounds [45, 46]. Hexagonal boron nitride and graphene present a unique option to create a GBN hybrid. For instance, thanks to their almost identical lattice constants, it is realizable to create layer-by-layer structural composition of graphene and h-BN [47, 48]. Utilizing different precursor molecules, efforts have been made to experimentally create GBN through chemical vapor deposition [49, 50]. This would let researchers tailor the electronic properties of graphene-based structures. Liu et al. [23] employs chemical vapor deposition (CVD) method and lithography technique to produce Graphene/h-BN lateral heterostructure with regular arrangement of h-BN and graphene domains. With plasma-assisted fabrication techniques [22], single and multiple layer of graphene could be built epitaxially on h-BN[22]. The magnetism [50], the strong half-metallic nature [51] and extraordinary thermal transports [52] give GBN hybrid structure unique physical properties. Thus, the future of nanoelectronics will likely depend on its huge potential applications [53].

Additionally, the shape of interface between h-BN and graphene [55, 59] influences the electronic properties of GBN nanosheet. Therefore, the most important region of interest is the interface between h-BN and graphene. There are variety of design to achieve maximum interface area between the h-BN and graphene region. In my thesis research, a diamond shaped island is used for both h-BN and graphene layout. **Figure 3** shows various interfaces formed between graphene and h-BN domains to study the interface effects on the electronic structure of GBN hybrid.

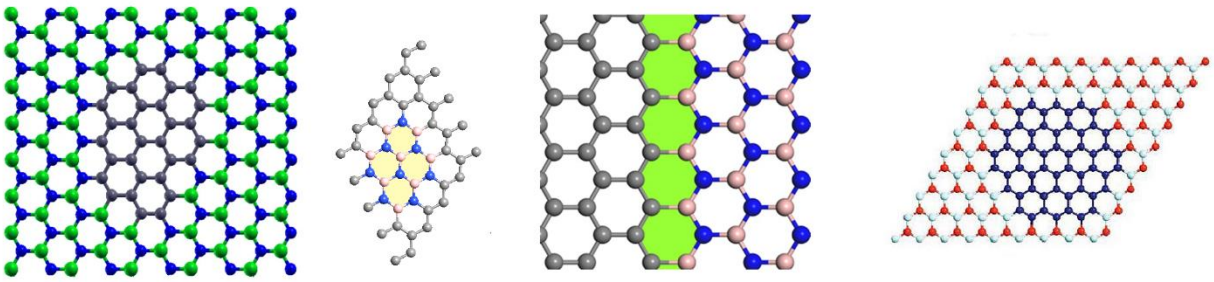

Figure 3 (a) Octagonal shaped interface with graphene island [59], (b) quadrilateral shaped interface with diamond shaped island, (c) linear interface between G and h-BN [55], (d) hexagonal shaped interface with graphene island [60].

The sensitivity of the gap between the layers of graphene is demonstrated to affect its electronic structure. With the help of energy gap engineering, a deposited graphene on a substrate can open the gap at the Dirac point, and this will accelerate the transfer rate of electrons on in this bilayer structure. The substrate that is most likely to host graphene is h-BN because of their near similar atomic arrangement. Latest Simulation in Molecular Dynamics [61] demonstrated that the N-C and B-C bonds around the interface of GBN hybrid improve the mechanical and electronic properties. Theoretical studies showed that the band gap can be tuned by putting an h-BN layer onto a graphene substrate [62].

1.4 Imperfection in solid

Since early 1900 crystallographers have been making effort to uncover the atomic arrangement in crystalline solid. At the beginning of the adoption of this method to crystalline structural analysis it become obvious that there is a need to differentiate between (i) crystals that are purely perfect and (ii) ideally imperfect ones, meaning there are some minute disorientation in their structural arrangement. If defect is formed in a three-dimensional crystal without inducing any external atoms, this type of defect is called intrinsic defect. Several kinds of dimensionalities exist for a nanostructured intrinsic material. Example of zero-dimensional materials includes point defect, whereas for line defect we have to talk about dislocation that originated from one dimensional line defect. While those that form in two dimensions are called stacking fault or grain boundaries. External atom can be defined as a zero dimensional defect. It occurs in a crystal when an external atom fills-in a vacancy site or when an external atom is introduced on interstitial sites. Understanding the magnetic and electronic properties of defective GBN hybrids can open the way for producing new materials with potential of applications. Introducing a single vacancy into the graphene can enhance its chemical sensing capabilities [63]. Manipulation of magnetism in system with vacancy draw the attention of many researchers to the area of its spintronic applications.

1.41 Defect in graphene

Many experimental studies prove the presence of vacancy defects in graphene nanostructure. Apart from the inherent structural defects that may occur during production, graphene gets modified by introducing external atoms such as boron or nitrogen. Fabrication of graphene nanoribbon and doping it with nitrogen was made by employing electrical heat on ammonia to produce an n-type FET that works at an ambient temperature [64]. The defects such as mono and multiple defects, topological defect, and carbon adatom in single walled and mono layer graphene carbon nanostructure can be produced via electron beam irradiation [65]. In the spectroscopy x-ray analysis, it is possible to dope boron atom into graphene through a controlled thermal heating approach. The resulting structure has a potential application in advanced nanoelectronics devices [66]. By employing electron/ion beam irradiation, single vacancy defect could be created on the surface of graphite, the magnetic moment could be observed around the single vacancy defect and the electrons localize at the Fermi level [67].

1.42 Defect in hexagonal boron nitride

During the crystal formation and processing, defects such as structural, SW, and vacancy defect are often appeared unintentionally. In many cases the defect can be a liability to the mechanical, thermal and electronic properties of the nanostructures. But still the defected systems are highly regarded for their potential application in advanced electronics. Defect in h-BN is of particular interest to researchers for their ability to emit a single-photon, therefore it draw a huge interest as a medium for spintronic and quantum information applications. For nano communication devices and semiconductor applications, h-BN is the prepared choice for wide energy band related applications. Van der Waals forces held hexagonal boron nitride layers together in the bulk sample, this makes the possibility of exfoliating the layers mechanically to an atomically thin sheet of nanostructure and the ability of its native defect to emit single photon at room temperature. Without producing excitonic emission, defect can still exist in h-BN structure [68]. The preparation and fabrication of a single layer h-BN almost always left an unintentional defect on the system. Defect was introduced into a pristine h-BN powdered sample mechanically using a ball-mill.[41]. After characterizing the defected h-BN, the result shows a correlation between increasing reaction

efficiency with amine group and improving defect size concentration of the hexagonal boron nitride nanosheet.

1.4.3 Defect in graphene/hexagonal boron nitride

While the properties of GBN hybrid structures are similar to boron nitride and graphene, they have caught the attention of many research groups very recently, because of their further amazing properties and applications [69]. By combining the pristine boron nitride and pristine graphene, a new material with a tunable band gap can emerge. The terms “pristine” and “defect-free” will be used interchangeably throughout the text. The former could be best use to describe systems that are in their original condition; clean, fresh, and spotless (mostly use on graphene and h-BN). While the later could also hold the same description, but it will mostly be use on GBN systems. Several researchs were conducted in recent years to investigate the presence of defect and holes in these two amazing materials, either in pure or in hybrid form [70]. A lot of resources had been put in place for analyzing the properties of defect-free and defected graphene and h-BN using molecular dynamic simulation. In this thesis, the embedded atoms replace certain number of carbon atoms (or B and N atoms) in order to form a diamond shaped island.

In recent years, the idea of intentionally introducing defect on boron nitride and graphene materials at different circumstances and for several of uses have caught the attention of multiple researcher groups. Therefore, making it very critical to acknowledge the effects of the defect on GBN hybrids on their electrical, structural, and magnetic properties. The most important region for a defect to be situated in the GBN nanosheet is the interface. It is therefore of very important to study the effect of vacancy at this location. It should be noted that the defect at the interface could be formed during the preparation and synthetization processes or later during the use of the hybrid. Binding forces between atoms are weaker at the boundary and the defect could functionalize the system.

1.5 Density Functional Theory

Density functional theory (DFT) is a computational method of approximately solving many body Schrodinger equation. Magnetic, Electronic and structural properties of many body systems can be explore using DFT. It is one of the well-known and adaptable process that are ready for use in

computational chemistry, computational physics, and condensed-matter physics. From computational material science perspective, the first principle DFT calculation enables the forecasting and computation of material quantum mechanical properties, without the need for important parameters such as fundamental material properties.

A comprehensive quantum analysis of material would certainly require the computation of the system's many nuclei, many-electron wave function. The dynamics of nuclei and electrons are critical in finding the right solution. The Born Oppenheimer approximation make things a bit simpler by proposing a theory that says, nuclei are large, heavy, and move slowly while electrons are smaller and faster. That means one can separate the dynamics of the nuclei and electrons. Therefore, the duration electrons need to settle for the ground state with one particular position of the nuclei, is quicker than the nuclei are able to respond. So, what the electrons will only see is the external potential of the stationary nuclei. The lowest of all the energy states is that of ground-state and is the most stable. The heart of DFT is based on two underlying theorems from Kohn and Hohenberg. They Came up with the way to obtain the ground state of electron density. The technique is to consider a set of single that are not interactive to electron wave functions.

1.5.1 Derivation and formalism

The nuclei of a target cluster or molecule in , many body electronic structural computations are treated as stationary, creating and external potential *P* that is static, whereas the electrons can move freely. Electronic mode that is static is then expressed by a wavefunction $\Psi(r_1, \ldots\ldots, r_N)$ fulfilling the Schrödinger equation of many electron system that is independent on time.

$$H\Psi = [\mathcal{T} + V + U]\Psi = \left[\sum_i^N \left(-\frac{\hbar^2}{2m_i}\nabla_i^2\right) + \sum_i^N V(r_i) + \sum_{i<j}^N U(r_i, r_j)\right]\Psi = E\Psi,$$

The variable *T* and U are referred to as universal variables, like wise for any system with N number of electrons, while the value of V depend on the system. Due to the interaction term U, the compounded many body equations could not have been divided into uncomplicated single particle.

In calculating the many particle Schrödinger equation there are numerous complicated processes that exist based on the Slater determinants wavefunction expansion. While there are some complicated methods like post Hartree–Fock, straightforward methods are commonly classified Hartree–Fock. Nonetheless, the issue with these approaches is the enormous computational power they require, which make them extremely difficult to work with and to provide accurately to a bigger, and more complicated nanostructures.

The electron density $n(r)$, is the primary variable in the DFT that's given by the equation below after normalization.

$$n(r) = N \int (d^3) r_2 .. \int (d^3 r_N) \Psi^*(r, r_2 .., r_N)(r, r_{2,} .., r_N) \Psi.$$

It is possible to reverse the expression above for $n_o(r)$, it is also realizable for the ground-state wavefunction $\Psi_o(r_1, .., r_N)$ to be computed [71].

$$\Psi_o = (\Psi)[n_o],$$

O is also a function to be observe with regards to the ground state expectation values of n_0

$$O[n_o] = \langle \Psi[n_o] | O | \Psi[n_o] \rangle.$$

specifically, the energy could be express as a function of n_0:

$$E_o = E[n_o] = \langle \Psi[n_0] | \mathrm{T} + \mathrm{V} + \mathrm{U} | \Psi[n_o] \rangle,$$

the external potential $\langle \Psi[n_o] | \mathrm{V} | \Psi[n_o] \rangle$ can be express as

$$V[n_o] = \int V(r) n_o(r) d^3 r.$$

Part of the external potential $\Psi|\mathrm{V}|\Psi$ can be written as a function of n

$$V[n] = \int V(r) n(r) d^3 r.$$

The terms that are called universal functionals are U[n] and U[n], the non-universal one is termed V[n], as it counts on the system being investigated. There are also other special characters like $\hat{V}$ that has the tendency of minimize the system.

$$E[n] = T[n] + U[n] + \int V(r)n\,(r)d^3r$$

Related to $n(r)$, suppose there is authentic interpretation for U[n] and T[n]. To determine the ground state density n_0 and other variables, a triumphant reduction of the energy functional is needed.

By employing the method of Lagrangian of multipliers undetermined.[72], the differential difficulty of reducing the energy functional E[n] will be resolved. At the beginning, it is appropriate to keep in mind that the energy functional does not clearly have an interaction of electron-electron energy state,

$$E_s[n] = \langle \Psi_s[n]|\mathrm{T} + \mathrm{V}_s|\Psi_s[n]\rangle,$$

where V_s denote an external potential that has the molecules moving, so that $n_s(\mathrm{r}) \stackrel{\text{def}}{=} n(r)$, while T stand for the kinetic-energy variable.

Hence, Kohn–Sham equations can be resolve for this supplementary noninteracting system,

$$\left[-\frac{\hbar^2}{2m}(\nabla^2) + V_s(r)\right](r)\varphi_i = \varepsilon_i(r)\varphi_i,$$

The outcome gives the φ_i as the orbitals that yield $n(r)$ as the density of the actual many body systems

$$(\vec{\boldsymbol{r}})\boldsymbol{n} \stackrel{\text{def}}{=} (\boldsymbol{r})\boldsymbol{n_s} = \sum_{\boldsymbol{i}}^{\boldsymbol{N}} |(\boldsymbol{r})\boldsymbol{\varphi_i}|^{\boldsymbol{2}}.$$

The actual potential of a single particle can be shown in more elaborative way as

$$(\boldsymbol{r})\boldsymbol{V_s} = (\boldsymbol{r})\boldsymbol{V} + [(\boldsymbol{r})\boldsymbol{n_s}]\boldsymbol{V_{XC}} + \int \frac{\boldsymbol{e^2 n_s(r')}}{\boldsymbol{|r - r'|}} \boldsymbol{d^3 r'},$$

1.5.2 Approximations

The precise functionals for correlation and exchange and are still unknown, and this is one major challenge faced in DFT. Nonetheless, there is precise computation of some physical quantities [73], using appropriate approximations. Among the major approximation technique is LDA, in which the function relies solely on the coordinate density where the function will be evaluated.

$$E_{XC}^{LDA}[n] = \int \varepsilon_{XC}(n) r(n(r) d^3).$$

The straightforward simplification of LDA that comprise of electron spin is local spin density approximation LSDA:

$$E_{XC}^{LSDA}[n_\uparrow, n_\uparrow] = \int \varepsilon_{XC}\,(n_\uparrow, n_\uparrow) n r(r) d^3.$$

The exchange correlation energy in LDA is commonly break down into the correlation part and the exchange part: $\varepsilon_{XC} = \varepsilon_X + \varepsilon_C$. The exchange section is referred to as the Dirac exchange, that is given as $\varepsilon_X \propto n^{1/3}$. The correlation section however takes other mathematical forms. From a simulations through quantum Monte Carlo [74], extremely precise formulae for the correlation energy density $\epsilon_c(n_\uparrow n_\downarrow)$ have been formulated.

The LDA made the assumption which says the density is distributed equally in all directions. Due to this, the LDA possess the capacity to overvalue the correlation energy and undervalue the exchange energy [75]. This enables adjustments established on the changes in density that are not close to the coordinate. These developments are called generalized gradient approximations (GGA) [77, 78] as given in the equation below:

$$E_{XC}^{GGA}[n_\uparrow, n_\downarrow] = \int \varepsilon_{XC}\,(\nabla n_\uparrow, \nabla n_\downarrow\, n_\uparrow, n_\downarrow,) r(r) d^3 n$$

Using the latter (GGA), there is an excellent outcome for ground-state energies and molecular geometries. There are likely better functionals then the GGA, for example meta-GGA functional.

DFT Meta-GGA functional in its initial format contains the second derivative of the electron density , while GGA contains just the derivative in the functionals of the exchange–correlation and its density. Challenges in explaining the exchange portion of the energy can be alleviated by conducting a section increase of the precise exchange energy computation from Hartree-Fock theory. Functional like this are celled hybrid functionals.

For the past 2 decades DFT has become a very important tool in chemistry [78]. Several research and studies in inorganic and organic chemistry regularly employ this kind of computations well known code, a normal functional approximation and normal basis [79] .Same development is taking place in material engineering where in the last 10 years advancement in both coding hardware made it feasible to carry out well-ordered comparison with experiment across vast scope of materials, knowing the right approximation to use and why, and enable the genuine first principle prediction of properties.

2.0 METHODOLOGY

The structure that has been studied is a combination of graphene and boron nitride in hexagonal form, in an in-plane nano sheet arrangement. Two distinct type of structures were studied. First, h-BN nanosheet layout as (substrate) hosting a graphene island in the shape of diamond, this structure will be referred to as G@h-BN. Second, graphene layout hosting a diamond shaped h-BN island referred to as h-BN@G. Both structures were fully analyzed, a full calculation was carried out. A though investigation was conducted to find the energetics of defective and defect-free GBN nanostructure by using DFT computations. Band structures of the GBN hybrid with varied types of vacancies was analyzed thoroughly. The computational protocol focuses on creating a single-atom vacancy at various locations on a GBN material and also to measure their local density of states at the nano level. It is demonstrated that a mono vacancy alters the electronic property of the system also how a mono atom vacancy plays a role in facilitating magnetization effects. Magnetism arises from vacancy defect was also investigated.

The calculation was adopted with GGA in conjunction with the (PW91) parametrization for the exchange correlation potentials [80]. Vienna Ab Initio Simulation Package (VASP, version 5.3) [82, 83] was the package used to conduct the electronic, DOS computations and geometry analysis. Projected augmented wave (PAW) techniques was employ to handle the electron-core interaction [83], [84]. Γ point centered Monkhorst-Pack grids was use carried out Brillouin zone Sampling. For partial occupancies of the orbitals two methods were employed (i) Methfessel-Paxton method was accepted in the first place because it yield more precise result of the total energy [85], (width of smearing is 0.1 eV) for the band structure calculations and geometry optimizations. (ii) k-point mesh convergence was performed for self-consistent computations, the non-self consistent DOS and energetics computations were performed by employing tetrahedron method [83].

For the convergence of optimum k-point mesh for geometric relaxation, the difference in the overall energy between two sequential loops is lower than $10\ \mathrm{meV}$. For pristine samples the optimum k-point meshes are listed as: Supercell of graphene: $4 \times 4 \times 1$, Unit cell of graphene: $10 \times 10 \times 3$, Supercell of h-BN: $3 \times 3 \times 1$, Unit cell of h-BN: $8 \times 8 \times 1$, vacancy defected and defect-free GBN supercells: $4 \times 4 \times 1$. or $3 \times 3 \times 1$.

Number of atoms in unit/supercells are 2/162 for pristine system and 2/161 for defective system. The geometries of the hybrids were optimized self-consistently. To minimize the external pressure to the unit of kB, with all its atoms together, optimization was carried out for the hexagonal the lattice vectors. Static self-consistent computation was carried out to get the total energy and charge density on the system following geometric relaxation. Non self-consistent computation was conducted for DOS and band of the optimized structures while self-consistent computation provides the charge density. Spin polarized (SP) calculations and spin unpolarized (NSP) were carried out for each of the defective and pristine system to ascertain their magnetic moment and ground state. SP DFT computations were performed for magnetic structures collinear in all steps outline above.

The super cell structures for both h-BN, graphene and defect-free GBN nanostructures has a hexagonal lattice of 9×9 super cells. Three distinct defect-free hybrids in total with different island size were optimized for each $G@h-BN$ and $h-BN@G$ hybrids. Their magnetic and electronic properties were evaluated using the DFT. For clarity through-out the text G-BN hybrids, is presented as $\mathrm{XG(D)@h-BN}$, involves a graphene (G) island in the shape of diamond of size X in the h-BN layout. While the B-NG is presented as $\mathrm{Xh-BN(D)@G}$, involves a h-BN island in the shape of diamond of size X in graphene (G) layout. The D inside the parenthesis means diamond/rhombic shaped island. The unit of the hexagonal shape is the smallest in the nanosheet structure, and hence X is therefore the total number of hexagons contained within the island. X is 4, 9 and 16 for the three different island sizes.

A mono vacancy is then formed by removing nitrogen or boron atom at the interface between h-BN layout and G island, additionally a vacancy of B or N and C is also created at the h-BN and G island for G-BN and BN-G hybrids respectively. A total of 42 defective hybrids were studied carefully. The notations for the vacancy types and their positions are as follows: (VC_{I1}) and (VC_{I2}) denote carbon single vacancy at the G-BN interface, with immediate neighboring atom being (nitrogen and carbon) and (boron and carbon) respectively. Additionally, single carbon atom was removed at the middle of neighboring carbon atoms designated as VC_i, the vacancy appears at the middle of graphene island for G-BN hybrids while it appears in the layout for BN-G systems. VB_L (VN_L) and VB_I (VN_I) denote to nitrogen (boron) single vacancies at the layout and in the interface respectively.

A 14 Å vacuum space was used to get rid of any unwanted interaction between successive layers of the hybrid. By employing conjugate gradient algorithm, the structures were instantaneously relaxed into their ground state. The calculated lattice parameters optimized using DFT (measured in Å) are as follows: Graphene supercell: C = 14.55, B = 2.21, A = 22.21. Graphene supercell having carbon atom removed: C = 15.60, B = 22.21, A = 22.11. Graphene unit cell: C = 10.00, B = 2.46, A = 2.46. (having primitive lattice vectors a_2 = 2.13 ŷ + 1.23 x̂. a_1 = 2.46 x̂). h-BN supercell: C = 14.00, B = 22.60, A = 22.60. h-BN supercell having boron atom removed: C = 11.49, B = 22.63, A = 22.60. h-BN unit cell: C = 13.99, B = 2.51, A = 2.51. (having primitive lattice vectors a_2 = 2.18 ŷ +1.26 x̂, a_1 = 2.51 x̂,). h-BN supercell having nitrogen atom removed: C = 14.00, B = 22.57, A = 22.57. Optimized lattice parameters of defect-free G-BN hybrids with differing length C = 14.00-14.52. B= 22.26- 22.58, A = 22.27-22.59. One may be curious as to why the value of lattice parameters were given in C, B, A sequence rather than the usual A, B, C. The values were given in that manner to avoid reporting a similar text from our recent publication [86]. The publication comes from the result of this thesis research.

2.1 The Vienna Ab Initio Simulation Package

The Vienna Ab initio Simulation Package, popularly called as VASP, is a computer program for performing nano level materials modelling either using projector augmented wave or the Vanderbilt pseudopotentials. The usual procedure is DFT, though the code enable modification even after the DFT, such method as Hartree–Fock exchange and mixing hybrid functionals. VASP employs well organized charge density mixing Broyden/Pulay and an effective matrix diagonalization scheme. This approach compliments the challenges faced with the initial method of Car-parrinello that comes from the simultaneous integration of ionic equations and electronic motions. Projector-augmented wave or ultra-soft Vanderbilt pseudopotential method were used to explain the relationship between electrons and ions.

Ultra-soft pseudopotential approximation and Planewave basis set were the dominant application being used even though the latest version has an all-electron option. For molecular applications, the Plane wave basis sets are to some extent distinctive, this is due to the connection of free electron with plane wave basis sets like systems. Surely, if the basis set is big enough, such connections cannot be supported. For example, VASP has been used extensively in exploring graphite,

diamond, carbon nanotubes, and various other electronic applications that chemical systems that are not free of electrons.

Another tool that we used to analyze the output files is Virtual Nanolab. Virtual Nanolab (VNL) is a commercial software for atomic-scale modeling and simulation of nanostructures, using classical interatomic potentials. It merges non equilibrium Green's functions with DFT for Ab initio electronic structures and transport computations of molecules, periodic system, and electrodes. The programming language is Python that simplifies the development and analysis of both normal and highly customized simulations. It can simulate, polymers, alloy materials, interfaces between materials, surfaces, complex crystalline and electronic devices with nanostructured sizes. The software defines structures at the atomic-scale and compute their chemical and physical properties. On the other hand, numerical optimization algorithms are very important concept in atomistic scale simulation, as optimization problems can be formulated by finding stable structures and reaction mechanisms.

3.0 RESULTS

A hexagonal boron nitride layout was prepared, and a diamond shaped graphene island of different sizes was implanted on it. Besides, a diamond shaped h-BN island of different sizes was also implanted on graphene layout. Our goal is to create a unique GBN nanosheet consisting of either h-BN island in G layout (h-BN@G) or G island in h-BN layout (G@h-BN). The G layout involving an h-BN island with size X is represented as Xh-BN(D)@G. We also represent the h-BN layout involving a G island with size X as XG(D)@h-BN. Here, X represents the size of the diamond shaped island, and X is 4, 9, or 16 in this thesis. X also represents the number of hexagonal units contained within the island. The D inside the parentheses means that the island is in the shape of diamond. The energetics of island implantation were explained in the subsequent section in detail, There are a lot of theoretical and experimental researches conducted on h-BN, graphene, and GBN hybrid to determine how their properties change when subjected to internal or external effects.
Vacancy defect was created by taking off a single N, C, or B atom in the GBN nanosheet. Magnetic moment, band gap energy and defect formation energy were all calculated. The magnetic and electronic properties of defective and defect-free in-plane GBN hybrids were also discussed. Magnetization energy ΔE_M is the difference in total energies between NSP and SP states of the system i.e.

$$\Delta E_M = E_{NSP} - E_{SP} \tag{1}$$

When ΔE_M is positive (negative) the system is said to have an SP (NSP) ground state. If the magnetization energy is large, the system is supposed to be stable against thermal fluctuations. Hybrids with larger magnetization energy are expected to show stronger resistance against thermal variations at predetermined temperatures. According to our calculations, most of our hybrids are stable at room temperature. The lowest magnetic energy for the defective and non-defective hybrids are 0.2 meV and 0.1 meV, respectively (see **Table 1**, **Table 4**, and **Table 5**).

3.1 Defect-free nanosheet of GBN hybrids

A defect free nanosheet of 9 × 9 unit cell was made of 162 total number of atoms irrespective of its constituents. It is clearly demonstrated that bulk hexagonal boron nitride possess indirect band gap [87]. The single crystal high quality hexagonal boron nitride nanosheet was reported to possess a band gap of about 5.9 eV [35, 89]. The GW approximation approach is highly considered to be one of the best procedures to evaluate the band gap of insulator and semiconductors with better precision. Band gap of h-BN was calculated in one of our previous publication as 4.59 eV [60]. The computed N-B bond length is approximately 1.45 Å, that is compatible with the literature [37]. As expected, graphene is proved to be a semi metal having a zero band gap. One of the popular approaches for producing a single layer h-BN is through mechanical exfoliation from layered hexagonal boron nitride. Elias et al. [89] uses high-temperature molecular beam epitaxial method to produce an excellent mono-layer h-BN substrate. They discovered that a single atomic layer of h-BN has a direct energy gap of 6.1 eV. According to results of optical spectroscopy, the h-BN has an indirect energy band gap of 5.96 eV [68]. Optimized geometries together with the energy band structures of pristine h-BN and graphene are presented in **Figure 4**.

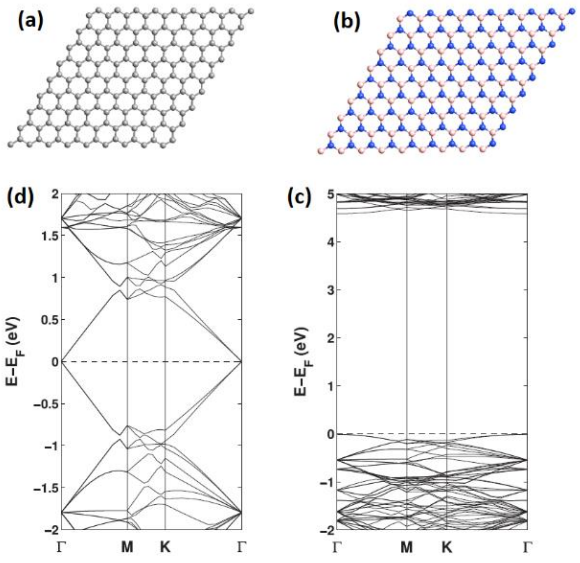

Figure 4 (a,b) Optimized geometries of pristine graphene and h-BN each with 162 atoms. Pink and blue colors show respectively boron and nitrogen atoms. Gray is used for carbon atoms. (c) Electronic band structure of pristine h-BN having a band gap of 4.59 eV (d) Electronic band structure of pristine graphene.

The tabulated magnetization energy, the total energy, band gap and magnetic moment of the defect-free GBN nanosheet were shown in **Table 1**. Moreover, the calculated ΔE_M is -3.20 meV for the graphene nanostructure and 0.4 meV for the h-BN nanostructure [90]. Both the h-BN and G possess nonmagnetic ground states. In defect-free hybrids, when the ΔE_M is less than 10 meV, they have NSP ground states that can simply be flipped to SP ones by exerting external influence such as increasing temperature. For G(D)@h-BN, the E_g value decreases as the G island increases. For h-BN(D)@G, the E_g value increases with increasing h-BN island. Optimized geometries of defect-free G(D)@h-BN and defect-free h-BN(D)@G were shown in **Figure 5**. The size of diamond shaped island (X) is 4, 9 or 16.

Table 1 System description and nomenclature are presented in the first and second column respectively. Total energy (E_T), magnetization energy (ΔE_M, equation (1)), magnetic moment (μ) and band gap (E_g) of the defect-free systems are tabulated in the third, fourth, fifth and six columns, respectively for both h-BN(D)@G and G(D)@h-BN. The first two rows are for the pristine h-BN and G, both of which are non-magnetic (NM).

System	Name	$E_T(eV)$	ΔE_M (meV)	μ (μ_B)	E_g (eV)
$B_{81}N_{81}$	h-BN	-	0.4	NM	4.59
C_{162}	G	-	-3.2	NM	0.00
$C_{16}B_{73}N_{73}$	4G(D)@h-BN	1432.60	-0.4	NM	2.13
$C_{30}B_{66}N_{66}$	9G(D)@h-BN	-1435.40	-0.1	NM	1.1
$C_{48}B_{57}N_{57}$	16G(D)@h-BN	-1439.70	0.4	NM	0.7
$C_{146}B_{8}N_{8}$	4h-BN(D)@G	-1483.90	0.10	NM	0.17
$C_{132}B_{15}N_{158}$	9h-BN(D)@G	-1475.53	-2.90	NM	0.36
$C_{144}B_{24}N_{24}$	16h-BN(D)@G	-1465.50	-2.90	NM	0.50

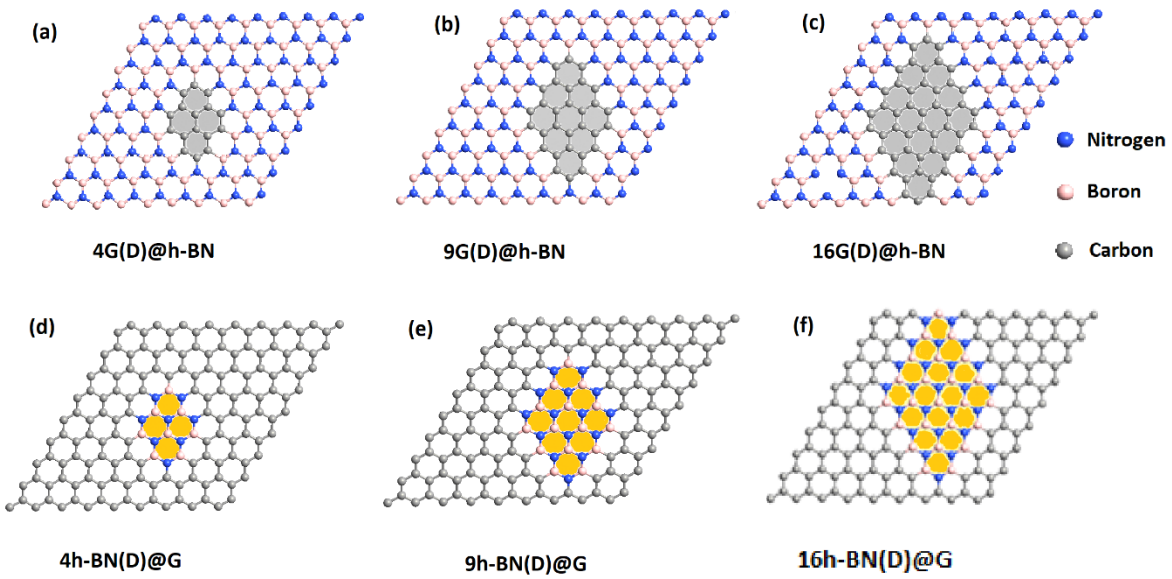

Figure 5 (a-c) Optimized geometries of defect-free G(D)@h-BN with diamond shaped graphene islands with sizes 4, 9 and 16. (d-f) Optimized geometries of defect-free h-BN(D)@G with diamond shaped h-BN islands with sizes 4, 9 and 16.

3.2 Energetics of island implantation

The chemical reactions to create the desired island on the substrate through solid state reaction between graphene and h-BN Equ. (2) layout and BN (C) cluster Equ. (3) is

$$h - BN_{162} + C_{Y+Z} \rightarrow G@h - BN + B_Y + N_Z \quad (2)$$

$$G_{162} + B_Y + N_Z \rightarrow h - BN@G + C_{Y+Z} \quad (3)$$

Mainly, implanting of an h-BN or graphene island into a planar system is not always a spontaneous ion implantation process. It is more like the islands to be embedded into different layers of bulk h-BN or graphite. The layers can then be exfoliated from the bulk sample. **Figure 6** shows the optimized structure of the defect-free GBN after island implantation for XG@h-BN. The figure also shows the band structures of systems. We obtained a proportional decrease in the energy gap as the island size increases. **Figure 7** also shows a similar representation for h-BN(D)@G. The band structural plots have a curvy contour unlike that of G(D)@h-BN that has flat bands. Like that

of G(D)@h-BN, the optimized geometry shows **a decrease** in the formation energy as the island size increases. The band gap increases with increasing size of h-BN island as tabulated in **Table 1**. Besides, the band gap decreases with growing G island.

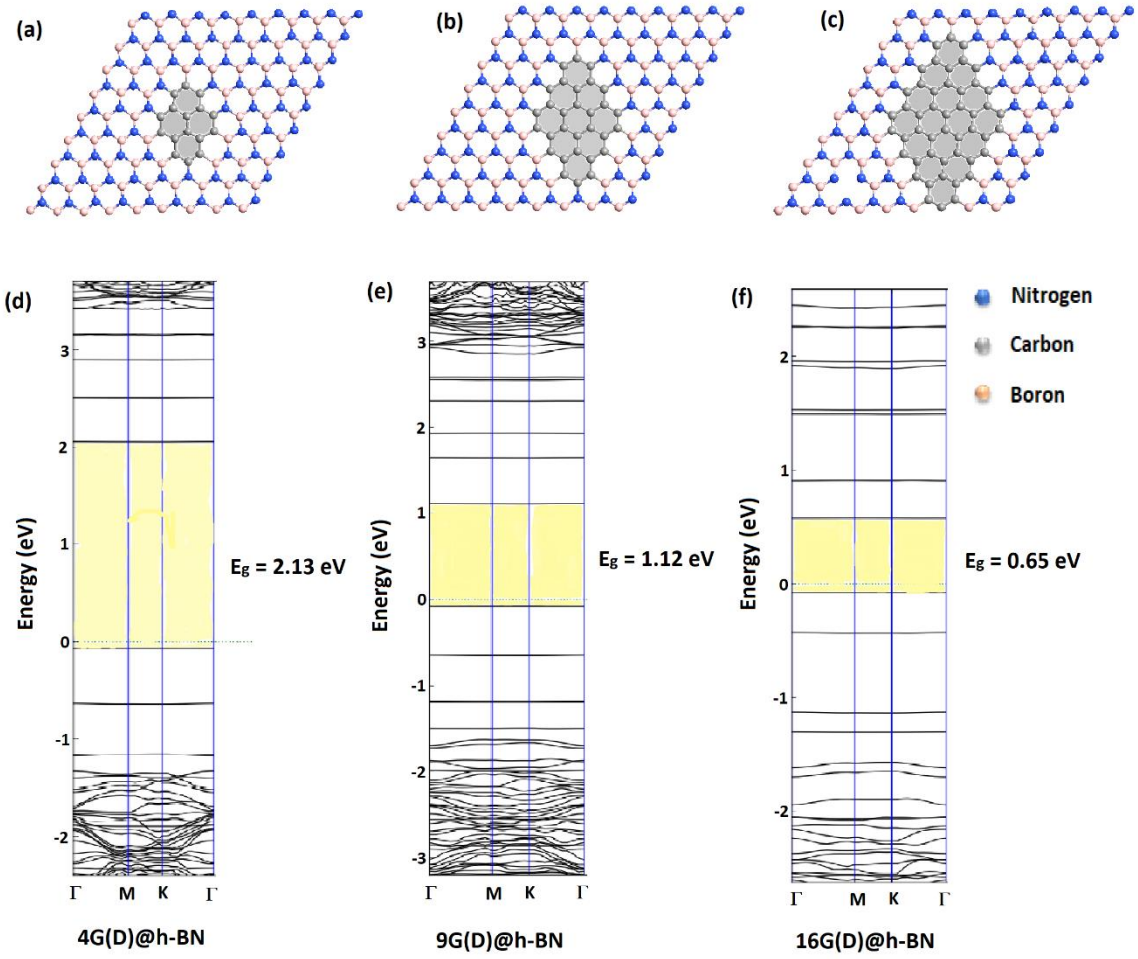

Figure 6 (a-c) Optimized geometries of the defect-free XG(D)@h-BN hybrids with sizes of island 4, 9 and 16. (d-f) Their NSP energy band diagrams. The G island is shown in gray color in optimized geometries. The yellow shaded portion in energy band diagrams is used to show the magnitude of E_g value. In energy band diagrams, the Fermi-level is indicated with a horizontal dotted line. There are 162 atoms in each defect-free hybrid.

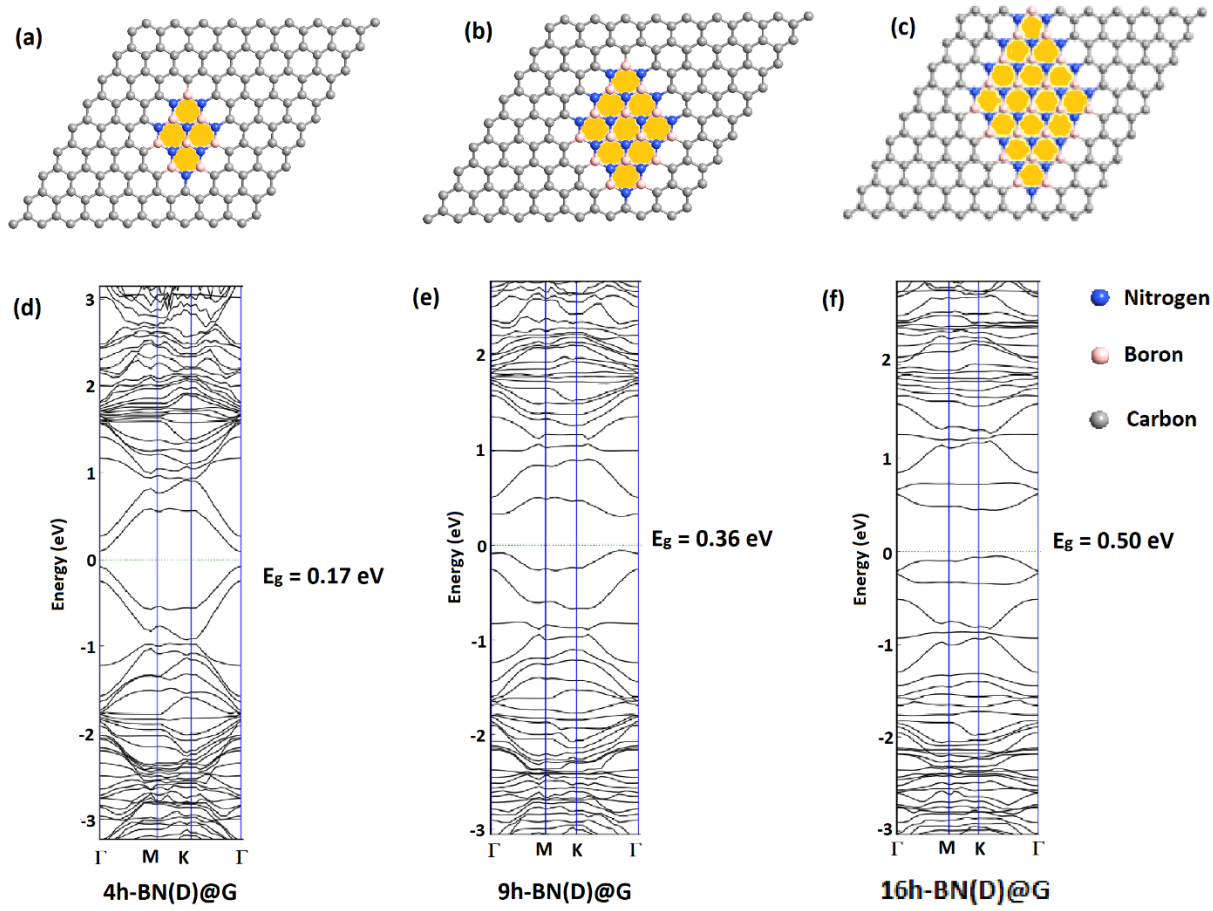

Figure 7 (a-c) Optimized geometries of defect-free Xh-BNG(D)@G hybrids with sizes of island 4, 9 and 16. (d-f) Their NSP energy band diagrams. The h-BN island is highlighted in yellow in optimized geometries. The E_g value of GBN hybrid increases as the size of h-BN island increases. In energy band diagrams, the Fermi level is indicated with a horizontal dotted line. There are 162 atoms in each defect-free hybrid.

E_f is the formation energy (i.e the total energy needed to create the island in the hexagonal layout) in this thesis. Energy per atom is the energy contribution from each atom that formed the island. The energy required for island formation decreases proportionally as the island size increases. Maximum ($\mathcal{E}_{if_{max}}$) and Minimum ($\mathcal{E}_{if_{min}}$), island formation energies of the defect-free hybrids were tabulated in **Table 2**. Ion implantation is considered as an endothermic process, though in some cases it might be considered as an exothermic. The minimum and maximum formation energies decrease with increasing island size X, for G(D)@h-BN and h-BN(D)@G systems.

$$E_f = (E_{h-BN@G} + (Y+Z) \times \mu[C]) - \left(E_{G_{162}} + \mu[B] \times Y + Z \times \mu[N]\right) \quad (2)$$

$$E_f = (E_{G@h-BN} + \mu[B] \times Y + Z \times \mu[N]) - (E_{h-BN_{162}} + (Y+Z) \times \mu[C]) \quad (3)$$

Table 2 System descriptions and the nomenclature were presented in the first and second columns, respectively. Energy per atom, the minimum $\mathcal{E}_{if_{min}}$ and maximum $\mathcal{E}_{if_{max}}$ island formation energy for defect-free GBN hybrids were presented in subsequent columns.

Hybrid	**Name**	**Energy (eV/atom)**	$\mathcal{E}_{if_{min}}$ **(eV)**	$\mathcal{E}_{if_{max}}$ **(eV)**	$\mathcal{E}_{if_{min}}$ **(eV/atom)**	$\mathcal{E}_{if_{max}}$ **(eV/atom)**
$C_{48}B_{57}N_{57}$	16G(D)@h-BN	-8.89	-311.65	356.59	-6.49	7.43
$C_{30}B_{66}N_{66}$	9G(D)@h-BN	-8.86	-193.58	224.07	-6.45	7.47
$C_{16}B_{73}N_{73}$	4G(D)@h-BN	-8.84	-102.23	120.52	-6.39	7.53
$C_{114}B_{24}N_{24}$	16h-BN(D)@G	-8.89	-334.70	334.000	-6.97	6.95
$C_{132}B_{15}N_{15}$	9h-BN(D)@G	-8.86	-207.70	210.20	-6.92	7.01
$C_{146}B_8N_8$	4h-BN(D)@G	-8.84	-109.50	113.30	-6.85	7.08

A recent publication [60], explained in details the solid state interaction of triangular and hexagonal shaped G-island and h-BN layout. Incident beam landing on the bulk sample supplies the required energy to break the local bonds. The formation energy, that is given in Equ. 2 and 3, outlines the possible pathway of reaction in a collision process. Applications of some chemical reactions within practicable energy ranges were considered without acknowledging the real experimental conditions. Formation energy was computed at zero pressure and temperature. Maximum and minimum formation energies are computed using the formulas in Equ. (4).

$$E_{if_{min}} = (E_{G@h-BN} + Y \times \mu[B_{bulk}] + Z \times \mu[N_{bulk}] - (E_{h-BN_{162}} + (Y+Z) \times \mu[C_{atom}])$$
$$E_{if_{max}} = (E_{G@h-BN} + Y \times \mu[B_{atom}] + Z \times \mu[N_{atom}] - (E_{h-BN_{162}} + (Y+Z) \times \mu[C_{bulk}])$$

$$E_{if_{min}} = (E_{h-BN@G} + (Y+Z) \times \mu[C_{bulk}]) - (E_{G_{162}} + Y \times \mu[B_{atom}] + Z \times \mu[N_{atom}]$$
$$E_{if_{max}} = (E_{h-BN@G} + (Y+Z) \times \mu[C_{atom}]) - (E_{G_{162}} + Y \times \mu[B_{bulk}] + Z \times \mu[N_{bulk}] \quad (4)$$

Where $E_{h-BN_{162}}$ *and* $E_{G@h-BN}$ are respectively the total energies of pristine h-BN nanostructure and h-BN layout hosting a G island. And $E_{h-BN@G}$ and $E_{G_{162}}$ are the total energies of G layout hosting an h-BN island and graphene nanosheet, respectively. The chemical potentials that are calculated using DFT for bulk elements and free atoms are: $\mu[B_{atom}]$ = -0.26 eV, $\mu[B_{bulk}]$ = -6.68 eV/atom (α), μ[Natom] = -3.00 eV, $\mu[N_{bulk}]$ = -8.34 eV/atom, $\mu[C_{atom}]$ = -1.19 eV, $\mu[C_{bulk}]$ = -9.24 eV/atom (G). Total energies of free N, C and B atoms were computed using the same supercell and methods of computation. We adopted crystal structures of bulk nitrogen and boron given in Ref. [92, 93] to calculate their cohesive energies in units of eV/atom.

3.3 Defective GBN hybrid: defect formation

The system can be defective unintentionally either by nature during fabrication process or deliberately by particle irradiation. Incident ion beams supplies the needed force to break the bonds of the defect-free sample. The defect types and their positions were described in **Table** 3. Single vacancy defects are VB, VN and VC for a missing B, N and C atom, respectively. 7 distinct types of defect were pointed out for each GBN hybrid. For VN_I,(VB_I), and VN_L, (VB_L), one N(B) atom was removed from the interface of GBN hybrid, and h-BN island or h-BN layout of GBN hybrid, respectively. The missing C atom between the two C atoms and one N (B) atom at the G-BN interface was represented as VC_{I1} (VC_{I2}). Moreover, VC_i represents a missing C atom in the graphene island. To calculate the defect formation energy, we use the formula $E_{df}[D(i)]$ in Equ. (5).

$$E_{df}[D(i)] = E_{Total}[D(i)] - E_{Total}[D(0)] + \mu_Y \quad (5)$$

Where $E_{Total}[D(i)]$ is the total energy of the GBN hybrid with a single vacancy, $E_{Total}[D(0)]$ is the total energy of the defect-free system. Here, (i) indicates the number of missing atoms in the system. In this thesis $i = 1$ and it means that there is a mono vacancy in the hybrid system. When i = 0, the system is defect-free. μ_Y is the chemical potential of the missing lattice atom, and Y represents the missing C, B or N.

Table 3 The types of vacancies and their locations in the GBN hybrid. VC, VN and VB represent the C, N and B mono vacancies, respectively. Here, the subscript I means that the vacancy is at the interface of G and h-BN domains. The subscript L means that the vacancy is at the layout of GBN hybrid. The subscript i means that the vacancy is in the island of hybrid nanosheet.

Notation	Location of the Vacancy
VC_{I1}	C vacancy neighboring C and N atoms at the Interface
VC_{I2}	C vacancy neighboring C and B atoms at the Interface
VC_i	C vacancy in the G island neighboring C atoms
VN_I	N vacancy at the Interface neighboring C and B atoms
VB_I	B vacancy at the interface neighboring C and N atoms
VN_L	N vacancy in the h-BN layout neighboring B atoms
VB_L	B vacancy in the h-BN layout neighboring N atoms
VN_i	N vacancy in the h-BN island neighboring B atoms
VB_i	B vacancy in the h-BN island neighboring N atoms

3.3.1 Defective GBN hybrid with G island

All defect-free systems do not acquire magnetic moment; therefore, they are non-magnetic systems. Magnetic ordering could not be established in the pristine structures. For the sizes 4 and 9, the VN_L defect has a lower energetic cost than the VB_L It is noted that the formation energy of VC_{I2} is usually greater than that of VC_{I1}. From this result, it is confidently clear that C-N bond is stronger than C-B bond. The highest values of magnetic moment and magnetization energy were obtained for the VB_L defected hybrid when the island is in size 9 and 16. This will likely make them more attractive for spintronic and magnetic applications. The VB_I defected hybrid involving G island with size 4 has the largest value of ΔE_M. Besides, the highest ΔE_M was obtained for the VB_L defected hybrid as the G island is in size 9 and 16.

3.3.1.1 Structural stability

Optimized geometries of the most stable defective hybrids were shown in **Figure 8**. There is no notable reconstruction after the structural optimization but it is clear that the dangling bonds of atoms close to the defect are responsible for the local in-plane or out of plane distortion. We noted that the vacancy at the interface of G-BN hybrid has a smaller defect formation energy E_{df}. It is safe to say that the interface is energetically favorable position for the creation of single vacancy. With enlarging graphene island, the formation energies of VB_L and VC_{I2} decrease, whereas the formation energy of VC_{1I} does not change with varying island size X.

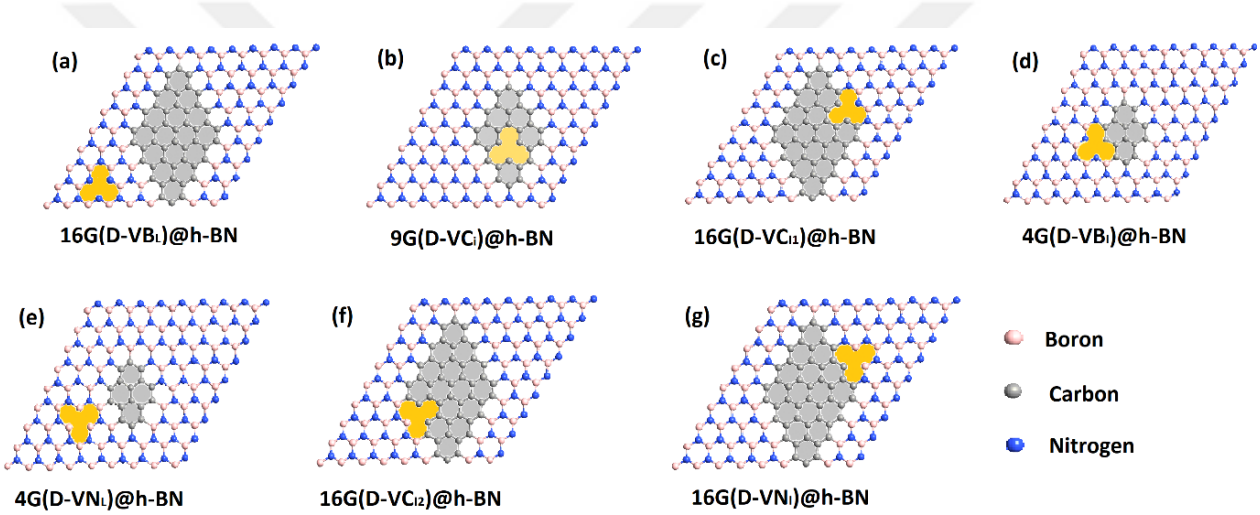

Figure 8. Optimized geometries of various vacancy defected GBN hybrids. The G island (shaded in grey) consists of 4, 9 or 16 hexagonal units. The mono vacancy is in the form of C, N and B. The vacancy region is highlighted in yellow color.

The optimized geometries of remaining defective hybrids are presented in **Figure 9**, **Figure** 10, and **Figure** 11. The magnetization energy increases with decreasing island size, for VN_L defect. Because of this result, it will be difficult to retain a constant magnetism in the VN_L defected system due to thermal fluctuations. Except for G size 9, the VN_I defected system has a significantly large magnetic energy. For the defect VB_I, the magnetization energy declines when the G size increases.

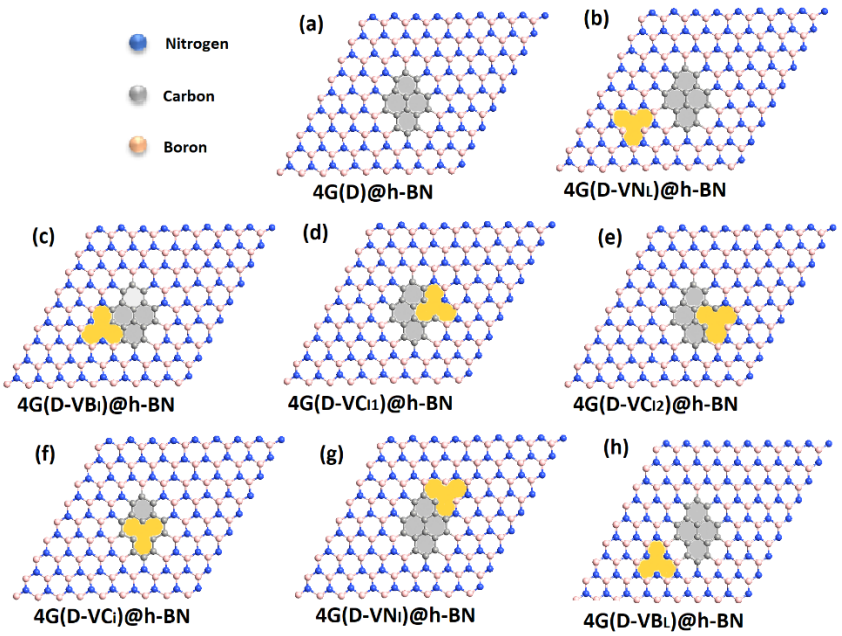

Figure 9 Optimized geometries of defect-free and defective GBN hybrids. The h-BN layout hosts a G island with size 4. The vacancy is shaded in yellow color. There are 161 atoms in each of the defective hybrids. The legend with color indication is shown at the top left corner.

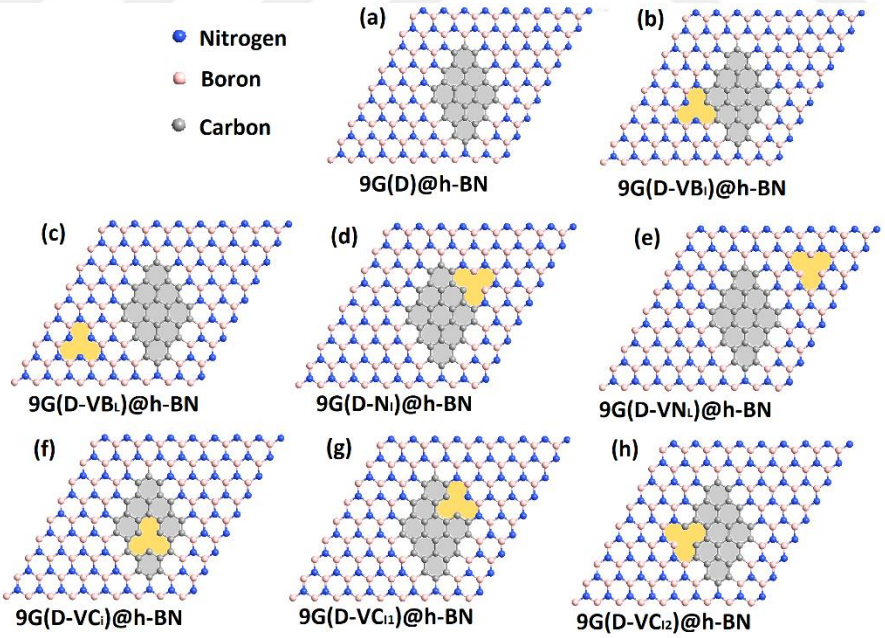

Figure 10 Optimized geometries of defect-free and defective GBN hybrids. The h-BN layout hosts a G island with size 9. The vacancy is shaded in yellow color. There are 161 atoms in each of the defective hybrids. The legend with color indication is shown at the top left corner.

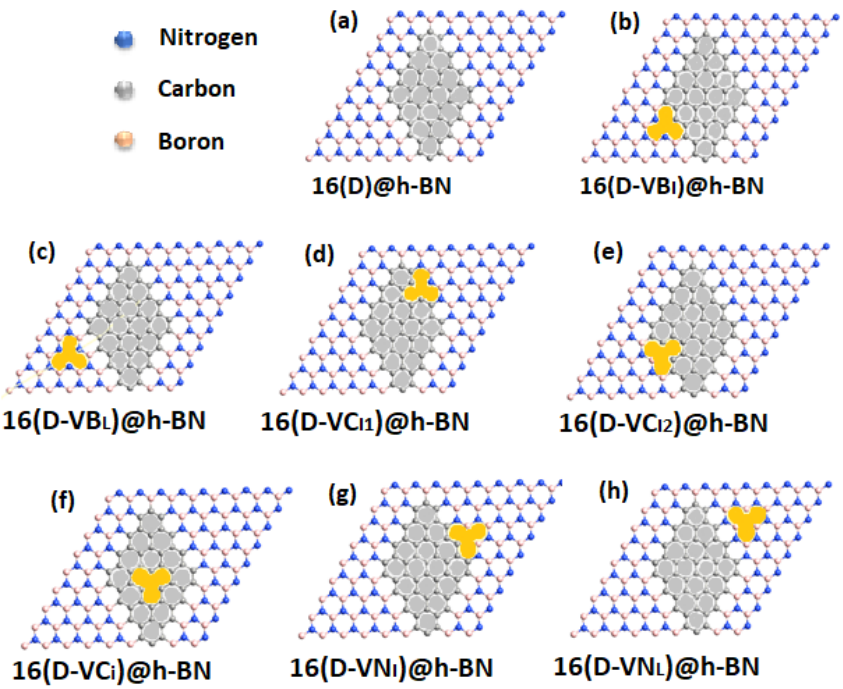

Figure 11 Optimized geometries of defect-free and defective GBN hybrids. The h-BN layout hosts a G island with size 16. The vacancy is shaded in yellow color. There are 161 atoms in each of the defective hybrids. The legend with color indication is shown at the top left corner.

For the vacancy defected hybrids, the defect formation energy (E_{df}), total energy (E_T), magnetization energy ΔE_M, band gap and magnetic moment values were presented in **Table 4.** For island sizes X = 4 and 9, the VC_{I1} defect renders a lower defect formation energy E_{df}. When the island is in size X = 16, VB_I shows a lower defect formation energy E_{df} based on the calculations. Additionally, with regards to VB defect, the energetically desirable vacancy is the VN for small sized G islands. However, the VB having a smaller E_{df} is energetically better option over the VN as the size of island is 16. In general, there is no correlation between the vacancy formation energy and island size. It is observed that while the magnetization energy (ΔE_M) of VC_i with G size 9 is negative, all the other defective hybrids have positive magnetization energies. The VC defected hybrids with G size 16 have no magnetic moments except for the hybrid having the defect VC_{I2}. As can be seen in **Table 4**, the VC_{I1} defected hybrids have small magnetization energies.

Table 4 Hybrids are displayed in the first column. The second column gives the nomenclature of the defective hybrids. The vacancy formation energy (E_{df} derived from Equ. (4)) is in the third column of the table for those hybrids displayed in **Figure 8**, **Figure 9**, **Figure 10**, and **Figure 11**). Fourth column renders the total energy values. Fifth and sixth columns display the magnetization energy (ΔE_M derived from Equ. (1)) and total magnetic moment (μ), respectively. ΔE_M is in unit of meV and μ is in unit of μ_B. NM signifies that the system has no magnetic moment or it is non-magnetic. The band gap (E_g) is in unit of eV and it is given in the last column.

System	Name	E_{df} (eV)	$E_T(eV)$	ΔE_M (meV)	μ (μ_B)	E_g (eV)
$C_{16}B_{72}N_{73}$	4G(D-VB_L)@h-BN	11.7	-1414.3	74.8	1.0	Metallic
$C_{16}B_{72}N_{73}$	4G(D-VB_I)@h-BN	8.4	-1417.5	294.9	-1.0	0.35
$C_{15}B_{73}N_{73}$	4G(D-VC_{I1})@h-BN	6.1	-1417.3	0.2	NM	1.3
$C_{15}B_{73}N_{73}$	4G(D-VC_{I2})@h-BN	6.5	-1416.9	99.8	NM	0.3
$C_{15}B_{73}N_{73}$	4G(D-VC_i)@h-BN	7.2	-1416.2	249.1	NM	1.0
$C_{16}B_{73}N_{72}$	4G(D-VN_L)@h-BN	7.7	-1416.5	103.2	1.0	0.4
$C_{16}B_{73}N_{72}$	4G(D-VN_I)@h-BN	7.1	-1417.2	260.8	1.0	1.1
$C_{30}B_{65}N_{66}$	9G(D-VB_L)@h-BN	9.4	-1419.3	615.7	3.0	0.02
$C_{30}B_{65}N_{66}$	9G(D-VB_I)@h-BN	8.6	-1420.2	82.4	-0.4	0.4
$C_{29}B_{66}N_{66}$	9G(D-VC_{I1})@h-BN	6.1	-1420.1	0.4	NM	1.2
$C_{29}B_{66}N_{66}$	9G(D-VC_{I2})@h-BN	6.5	-1419.7	45.9	NM	0.2
$C_{29}B_{66}N_{66}$	9G(D-VC_i)@h-BN	7.8	-1418.4	-194.3	2.0	0.5
$C_{30}B_{66}N_{65}$	9G(D-VN_L)@h-BN	7.8	-1419.3	99.8	1.0	0.2
$C_{30}B_{66}N_{65}$	9G(D-VN_I)@h-BN	7.2	-1419.3	38.1	1.0	0.2
$C_{48}B_{56}N_{57}$	16G(D-VB_L)@h-BN	6.4	-1424.0	549.8	3.0	0.2
$C_{48}B_{56}N_{57}$	16G(D-VB_I)@h-BN	5.9	-1424.5	16.1	1.0	0.02
$C_{47}B_{57}N_{57}$	16G(D-VC_{I1})@h-BN	6.1	-1424.3	0.7	NM	0.7
$C_{47}B_{57}N_{57}$	16G(D-VC_{I2})@h-BN	6.1	-1424.3	114.8	2.0	0.2
$C_{47}B_{57}N_{57}$	16G(D-VC_i)@h-BN	7.5	-1423.0	9.3	NM	0.5
$C_{48}B_{57}N_{56}$	16G(D-VN_L)@h-BN	7.4	-1424.0	43.9	1.0	0.03
$C_{48}B_{57}N_{56}$	16G(D-VN_I)@h-BN	7.0	-1424.3	210.6	1.0	0.6

According to our calculations, the VC_i defected hybrids do not have a magnetic moment. Regardless of island size, all defected VN hybrids have a total magnetic moment of 1 μB. Besides, the magnetic moment of VB_I defected hybrid increases (1 μB) when the G island grows in size. In a recent research [90], a total magnetic moment of 0.4 μB was obtained for the VC defected graphene nanosheet. This result is congruent with another work [93] given in the literature. The magnetic moment induced in VB_L defected hybrid increases with increasing size of G island.

3.3.1.2 Electronic band structure

The energy band diagrams of various defected hybrids were presented in **Figure** 12. The hybrids shown in **Figure** 12 are the vacancy defected hybrids having significant amount of magnetization energies. Besides, the calculated band gaps in these hybrids range between 0.2 to 0.5 eV. The band gap tuning in these hybrids could allow researchers to use them in many applications. As can be seen in **Table 4**, the band gap of VN_L defected hybrid decreases with increasing G size. From this result, we concluded that the VN_L defected hybrid can be converted from semiconductor to metal. The optimized geometry and energy band structure of system 9G(D-VC_i)@h-BN were respectively illustrated in **Figure 8(b)** and **Figure 12**(c).

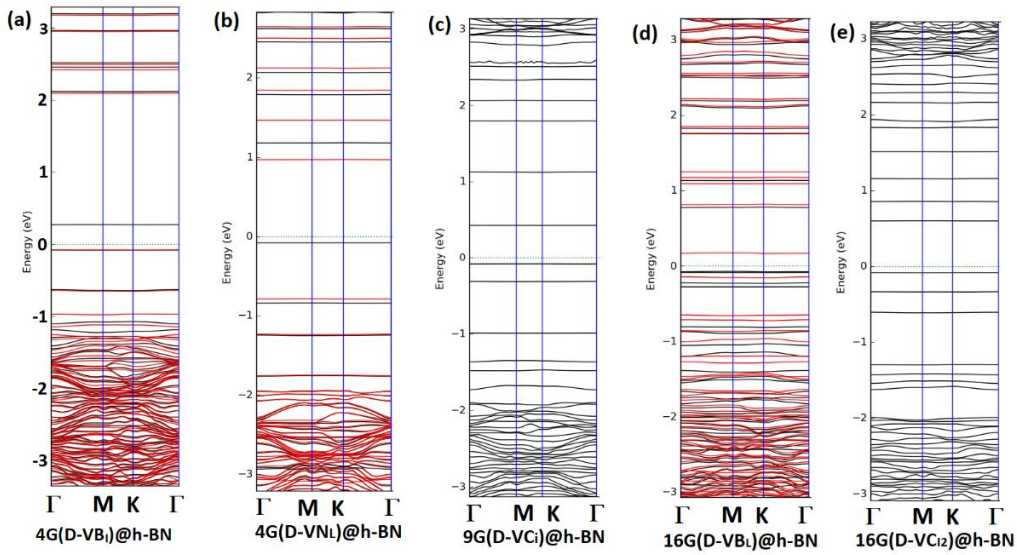

Figure 12 Electronic band structures of various hybrids shown in **Figure 8** with unique structural and electronic properties. The energy bands of spin up (spin down) electrons are shown in red (black). The defective hybrids have flat bands near the Fermi-level. Horizontal dotted line in green corresponds to the Fermi level.

The remaining systems show the same flat bands near the Fermi level, and their energy band structures are presented in (**Figure 13**, **Figure 14** and **Figure 15**). The flat band crossing the Fermi level of VB_L defected hybrid with G size 4 in **Figure 13** (b) makes this system a metal. The remaining hybrids display the characteristics of semiconductor.

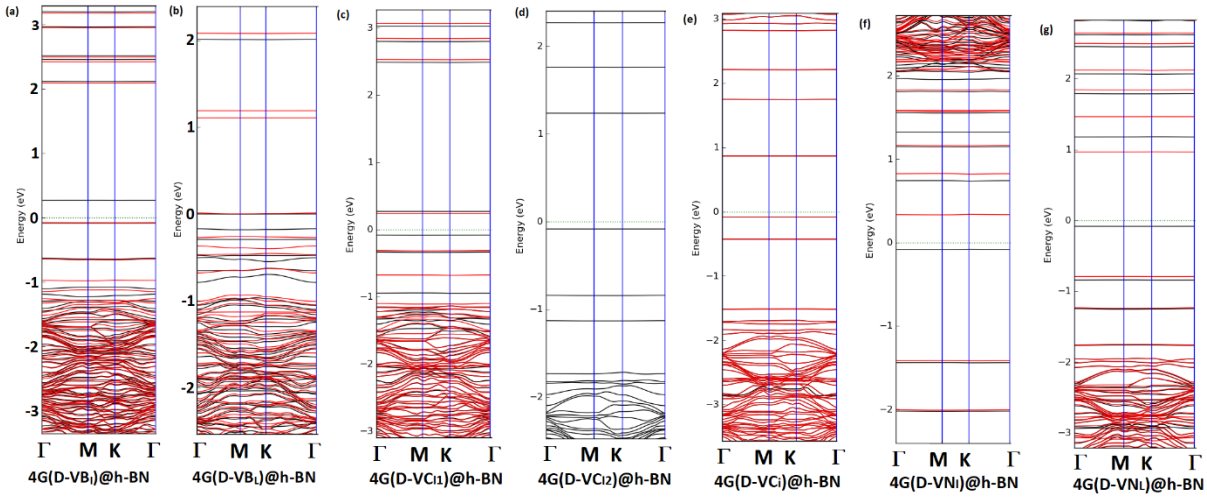

Figure 13 Electronic band structures of defective hybrids with G size 4. Spin splitting can clearly be noticed in these figures except for 4G(D-VC_{I2})@h-BN. The defective hybrids have flat bands near the Fermi-level.

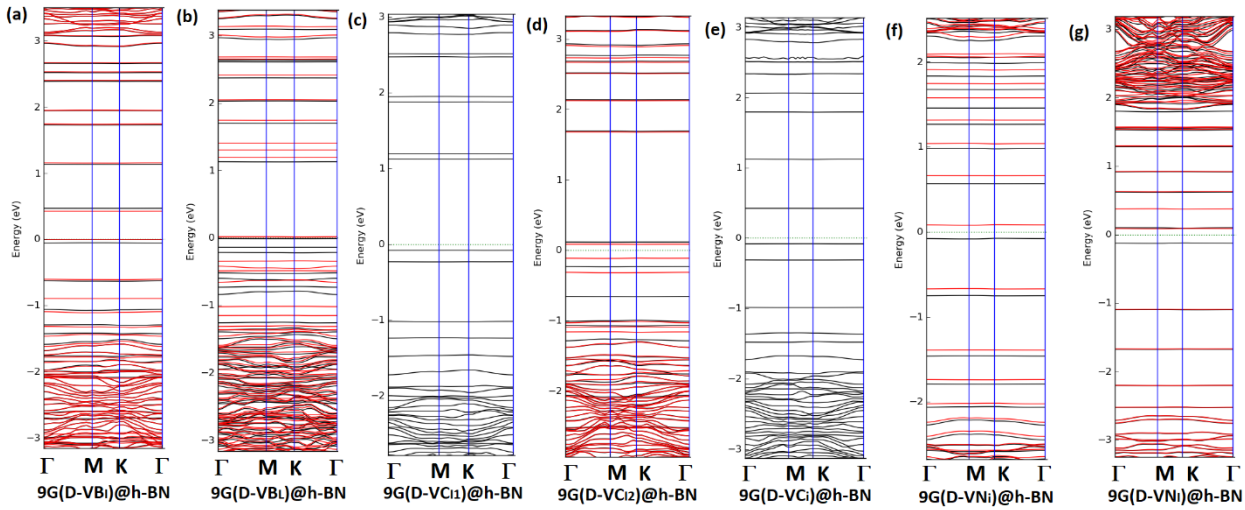

Figure 14 Electronic band structures of defective hybrids with G size 9. The defective hybrids have flat bands near the Fermi-level.

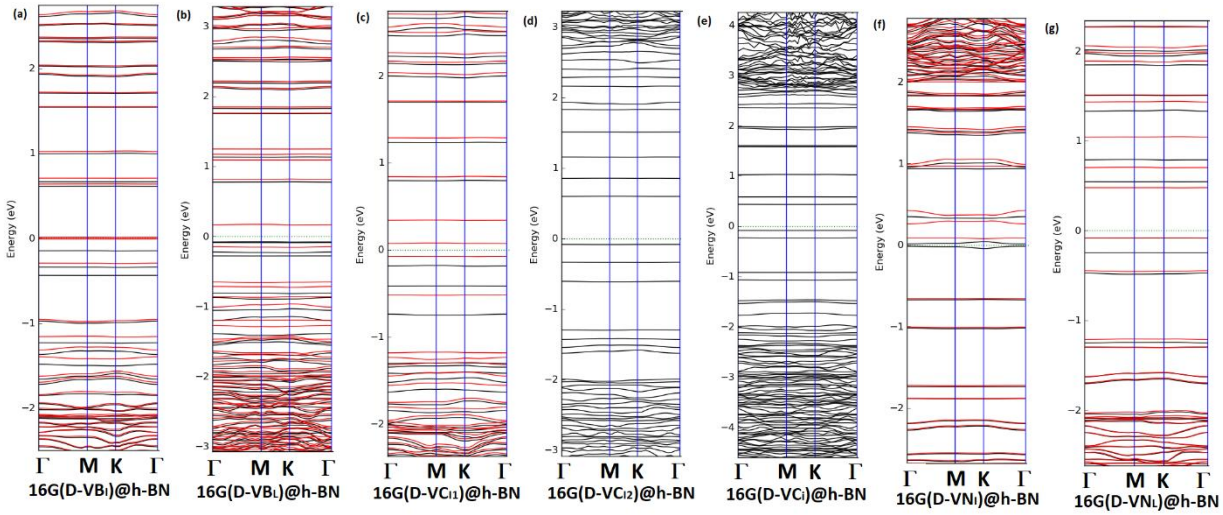

Figure 15 Electronic band structures of defective hybrids with G size 16. The defective hybrids have flat bands near the Fermi level.

The VB_L defected hybrid with G size 16 shown in **Figure 11** (c) has flat bands around the E_F. From the site projected band structural calculation shown in **Figure 16** and the spin density calculation shown in **Figure 17**, they have primarily σ character.

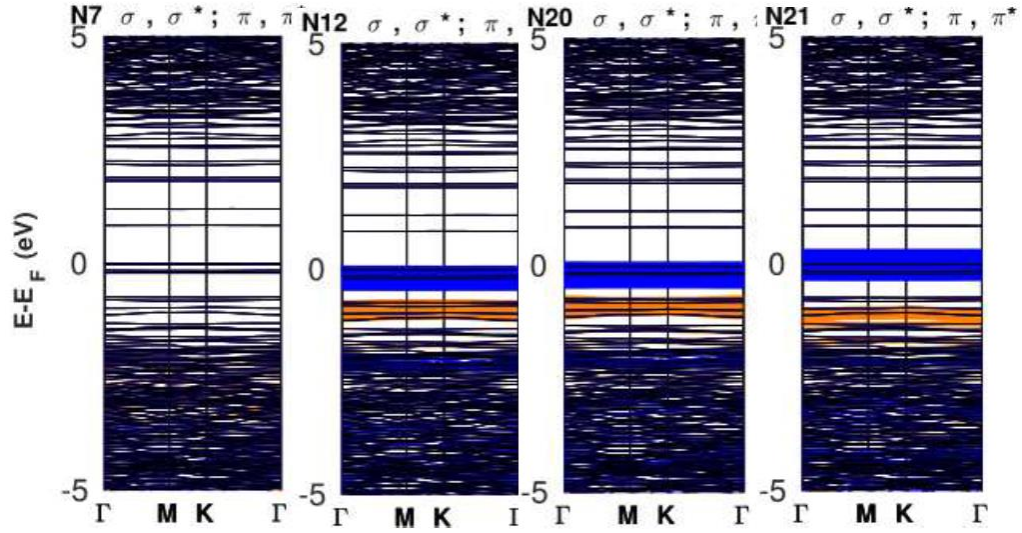

Figure 16 Site projected band structures of N7, N12, N20, N21 atoms in hybrid represented as 16G(D-VB_L)@h- BN. Energy bands with σ (π) character are shown in blue (orange). Unlike N12,

N20, N21 atoms, the N7 is further way from the vacancy site. Electronic behaviors of atoms far from the vacancy site are similar to that in N7.

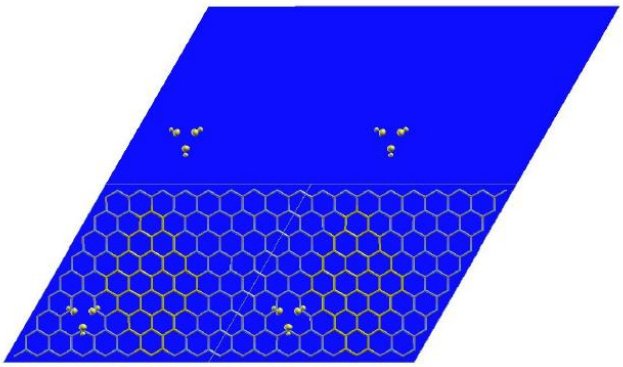

Figure 17 Spin density of hybrid represented as 16G(D-VBL)@h-BN. It is plotted at contours of 0.35 μB/Å^3.

Similarly, the energy band structure of hybrid 16G(D-VC_{I2})@h-BN was shown in **Figure 15** (d). It has a magnetic moment of 2 μB with an SP ground state. Its optimized geometry was given in **Figure 11** (e). We displayed its site projected band structure calculation in **Figure 18** and the spin density in **Figure 19**. From these plots we concluded that the states near the Fermi level show π and σ and characters.

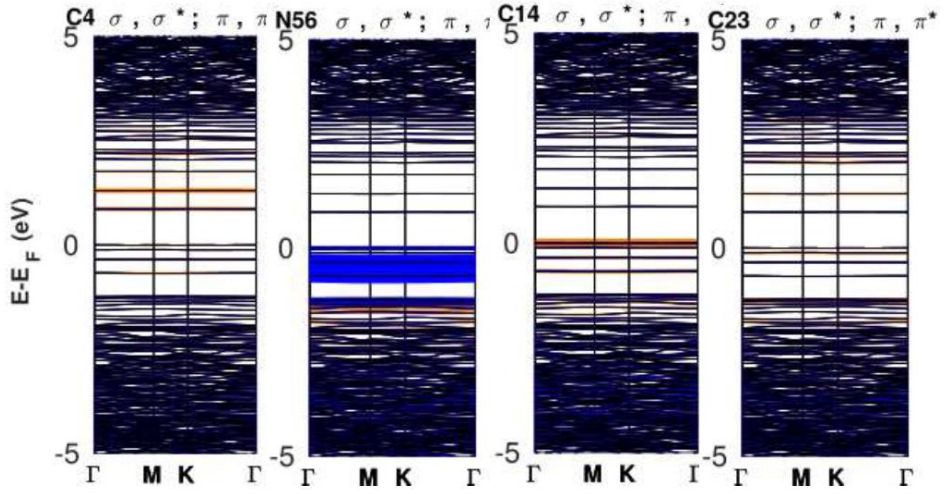

Figure 18 Site projected band structures of C4, N56, C14, C23 atoms in hybrid represented as 16G(D-VC_{I2})@h-BN. Energy bands with σ (π) character are shown in blue (orange). Unlike N56, C14, C23 atoms, the C4 is further away from the vacancy site. Electronic behaviors of atoms far from the vacancy site are similar to that in C4.

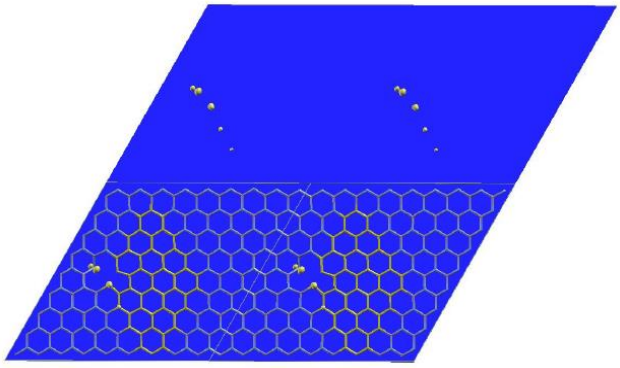

Figure 19 Spin density of hybrid represented as 16G(D-VCI2)@h-BN. It is plotted at contours of 0.15 μB/Å^3.

Irrespective of the size of the island, the VC_i defected GBN hybrid has no magnetic moment. Although the VC_i defected hybrid involving a G island with size 9 has NSP ground state, its ground state can easily be switched to SP one via external means such as thermal fluctuations. From the SP calculations, we obtained its magnetic moment as 2 μB and we presented it in **Table 4**. Its site projected band structures and spin density plot were illustrated in **Figure 20** and **Figure 21**, respectively. As seen in **Figure 20**, the flat bands emerge near the Fermi level E_F.

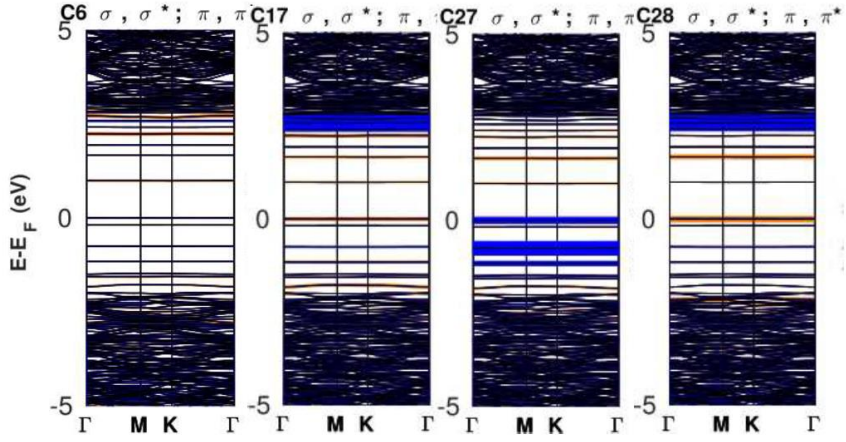

Figure 20 Site projected band structures of C6, C17, C27, C28 atoms for 9G(D-VC_i)@h-BN. Energy bands with σ (π) character are shown in blue (orange). Unlike C17, C27, C28 atoms, the C6 is further away from the vacancy site. Also, electronic behaviors of atoms far from the vacancy site are similar to that in C6.

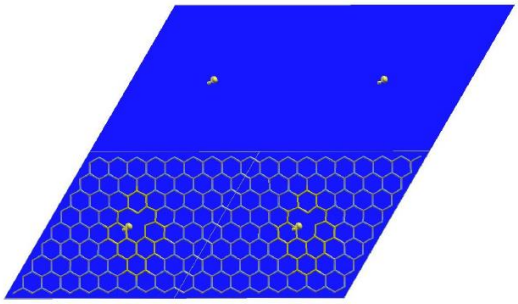

Figure 21 Spin density of 9G(D-VC_i)@h-BN. It is plotted at contours of 0.30 µB/Å^3.

3.3.2 Defective GBN hybrid with h-BN island

The defect formation energy, total energy, magnetization energy, total magnetic moment and band gap of defective GBN hybrids were shown in **Table 5**. The G layout includes a diamond shaped h-BN island with size X. The size of h-BN island (X) is 4, 9 and 16. The defect-free hybrid was represented as Xh-BN(D)@G. Defect-free hybrids do not acquire magnetic moment and therefore they are non-magnetic. It was observed that the magnetic moment (µ) of VC_{I1} defected hybrid with h-BN size 16 is negative. The remaining defective hybrids have positive magnetic moment values. The C vacancies at the interface of hybrids have no magnetic moments as the size of h-BN island (X) is 4. Likewise, the VN defected hybrids have no magnetic moments for the h-BN size 16. In case of X = 9 (4), the VC_{I2} and VN_I (VB_I) defected hybrids have also no magnetic moments. The VN_i defected hybrid has a magnetic moment of 1 μB as the h-BN size is 4 and 9. According to our calculations, we obtained a magnetic moment of 1.7 μB for the VC_L defected hybrid with h-BN size 4. Besides, its magnetic moment decreases to 0.3 as the island size increases. The highest value of magnetization energy was obtained for VB_i defected hybrids with island sizes 9 and 16. The VC_L defected hybrid with h-BN size 4 has the largest value of ΔE_M. We concluded that the hybrids with VB_i show a stronger magnetic stability and hence could be a better choice for device applications. For the case of VB_I, the magnetization energy decreases with increasing island size. The VB_i has the highest defect formation energy regardless of island size. However, the defect formation energy of VB_i increases with enlarging island. As the island size X = 9 and 16, the VC_{I2} defected hybrids have the lowest defect formation energies (E_{df}). For the island with size 4, the VC_{I1} defected hybrid has the lowest defect formation energy.

Table 5 Vacancy defected hybrids involving h-BN islands with size X are given in the first column. The nomenclature of the defective hybrids is given in the second column. In the third column, the defect formation energies (E_{df} derived from Equ. (5)) for hybrids displayed in **Figure 23**, **Figure 24**, **Figure 25** and **Figure 22** are given. The total energy is given in the fourth column. The magnetization energy (ΔE_M derived from Equ. (1)) and total magnetic moment (μ) are presented in the next two columns, respectively. The values of ΔE_M are given in unit of meV. The total magnetic moment (μ) is in unit of μ_B. Here, NM signifies that the hybrid has no magnetic moment or it is non-magnetic. The band gap (E_g) is given in the last column and it is in unit of eV.

System	**Name**	E_{df} (eV)	$E_T(eV)$	ΔE_M **(meV)**	**μ (μ_B)**	E_g (eV)
$C_{146}B_7N_{88}$	4h-BN(D-VB_i)@G	8.43	-1468.79	231.80	2.2	Metallic
$C_{146}B_7N_{88}$	4h-BN(D-VB_I)@G	7.30	-1469.92	9.90	NM	Metallic
$C_{145}B_8N_{88}$	4h-BN(D-VC_{I1})@G	5.63	-1468.99	3.20	NM	0.26c
$C_{145}B_8N_{88}$	4h-BN(D-VC_{I2})@G	6.81	-1467.85	42.40	NM	Metallic
$C_{145}B_8N_{88}$	4h-BN(D-VC_L)@G	7.71	-1466.95	300.80	1.7	Metallic
$C_{146}B_8N_{78}$	4h-BN(D-VN_i)@G	7.50	-1468.06	29.60	1.0	Metallic
$C_{146}B_8N_{78}$	4h-BN(D-VN_I)@G	6.91	-1468.65	-6.80	0.9	Metallic
$C_{132}B_{14}N_{158}$	9h-BN(D-VB_i)@G	8.45	-1460.40	545.2	2.0	Metallic
$C_{132}B_{14}N_{158}$	9h-BN(D-VB_I)@G	7.34	-1461.51	1.40	0.4	Metallic
$C_{131}B_{15}N_{1588}$	9h-BN(D-VC_{I1})@G	6.76	-1459.53	5.10	0.1	Metallic
$C_{131}B_{15}N_{158}$	9h-BN(D-VC_{I2})@G	5.61	-1460.68	29.70	NM	0.32
$C_{131}B_{15}N_{1588}$	9h-BN(D-VC_L)@G	7.67	-1458.62	144.8	1.5	Metallic
$C_{132}B_{15}N_{148}$	9h-BN(D-VN_i)@G	7.47	-1459.73	5.80	1.0	Metallic
$C_{132}B_{15}N_{148}$	9h-BN(D-VN_I)@G	6.81	-1460.38	-9.30	NM	Metallic
$C_{144}B_{23}N_{2488}$	16h-BN(D-VB_i)@G	8.96	-1449.86	665.9	2.0	Metallic
$C_{144}B_{23}N_{248}$	16h-BN(D-VB_I)@G	7.40	-1451.42	-1.60	1.0	Metallic
$C_{143}B_{24}N_{248}$	16h-BN(D-VC_{I1})@G	6.83	-1449.43	12.90	-0.4	Metallic
$C_{143}B_{24}N_{248}$	16h-BN(D-VC_{I2})@G	5.95	-1450.31	33.60	0.4	Metallic
$C_{143}B_{24}N_{2488}$	16h-BN(D-VC_L)@G	7.34	-1448.92	14.50	0.3	0.23
$C_{144}B_{24}N_{238}$	16h-BN(D-VN_i)@G	7.17	-1450.00	8.00	NM	Metallic
$C_{144}B_{24}N_{238}$	16h-BN(D-VN_I)@G	6.83	-1450.33	3.10	NM	Metallic

3.3.2.1 Structural stability

The defect formation energy did not change significantly with size of the h-BN island. The most stable defective hybrids are depicted in **Figure** 22.

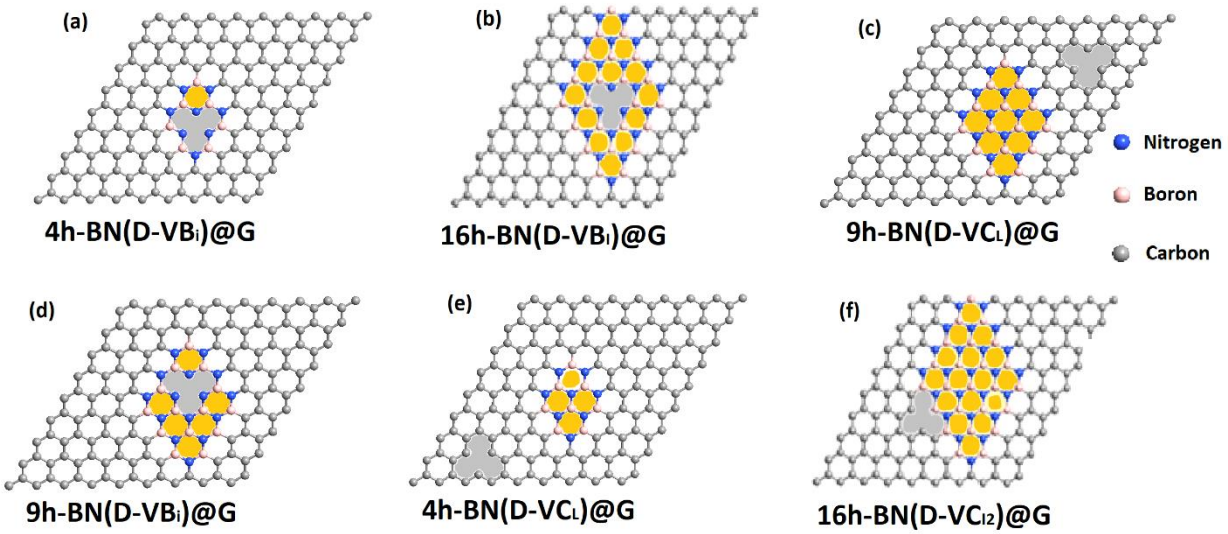

Figure 22 Optimized geometries of the most stable defective hybrids. (a) B vacancy in the h-BN island with size 4. (b) B vacancy in the h-BN island with size 16. (c) C vacancy in the G layout involving an h-BN island with size 9. (d) B vacancy in the h-BN island with size 9. (e) C vacancy in the G layout involving an h-BN island with size 4. (f) C vacancy neighboring B and C atoms at the interface of G and h-BN domains as the island is in size 16. Boron atoms are shown in pink and nitrogen atoms are shown in blue. C atoms are shown in gray. The size of diamond shaped h-BN island is 4, 9 or 16. The legend with color indication is shown at the bottom right corner.

The remaining defective hybrids hosting a diamond shaped h-BN island of different sizes were depicted in **Figure 23**, **Figure 24** and **Figure 25**.

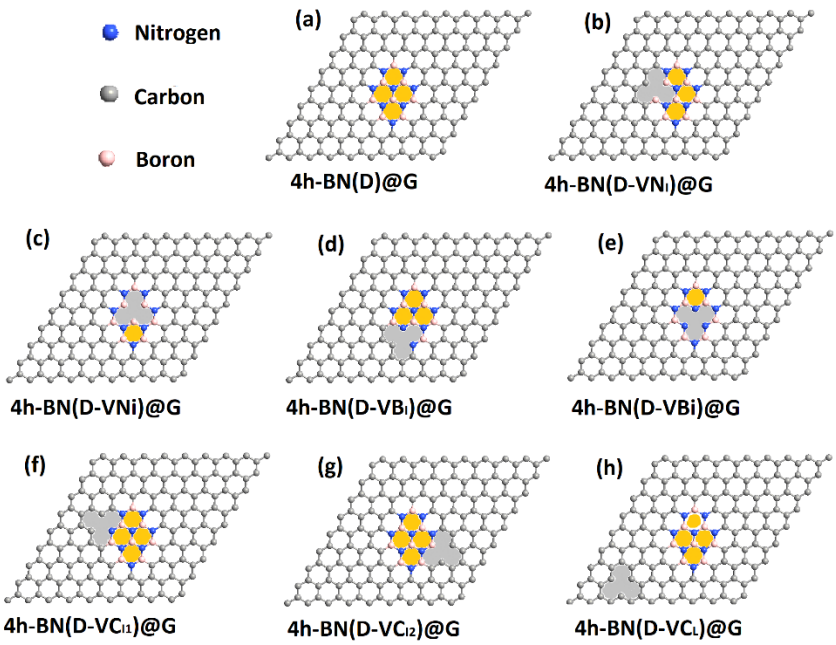

Figure 23 Optimized geometries of defect-free and defective GBN hybrids. The graphene layout hosts a diamond shaped h-BN island with size 4. The vacancy was highlighted in gray. The h-BN island was highlighted in yellow. The total number of atoms in each defective hybrid is 161. The legend with color indication is shown at the top left corner.

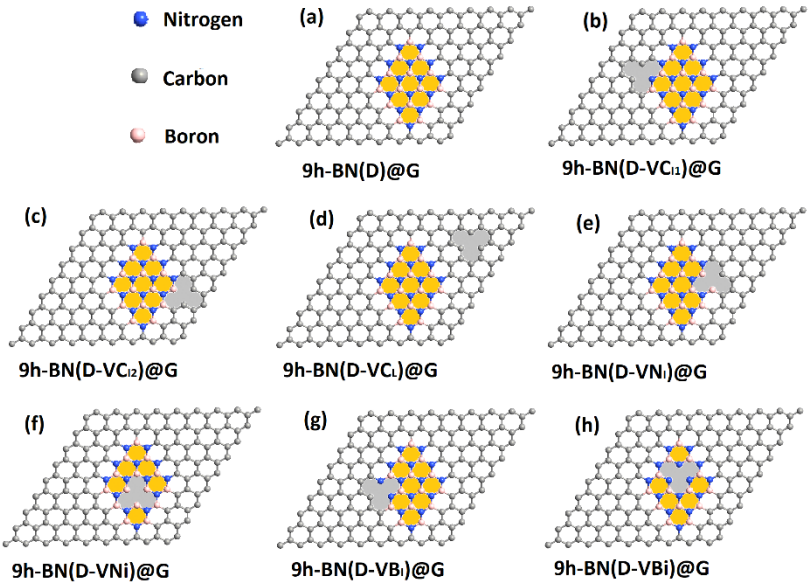

Figure 24 Optimized geometries of defect-free and defective GBN hybrids. The graphene layout hosts a diamond shaped h-BN island with size 9. The h-BN island was highlighted in yellow. The vacancy was highlighted in gray. The legend with color indication is shown at the top left corner.

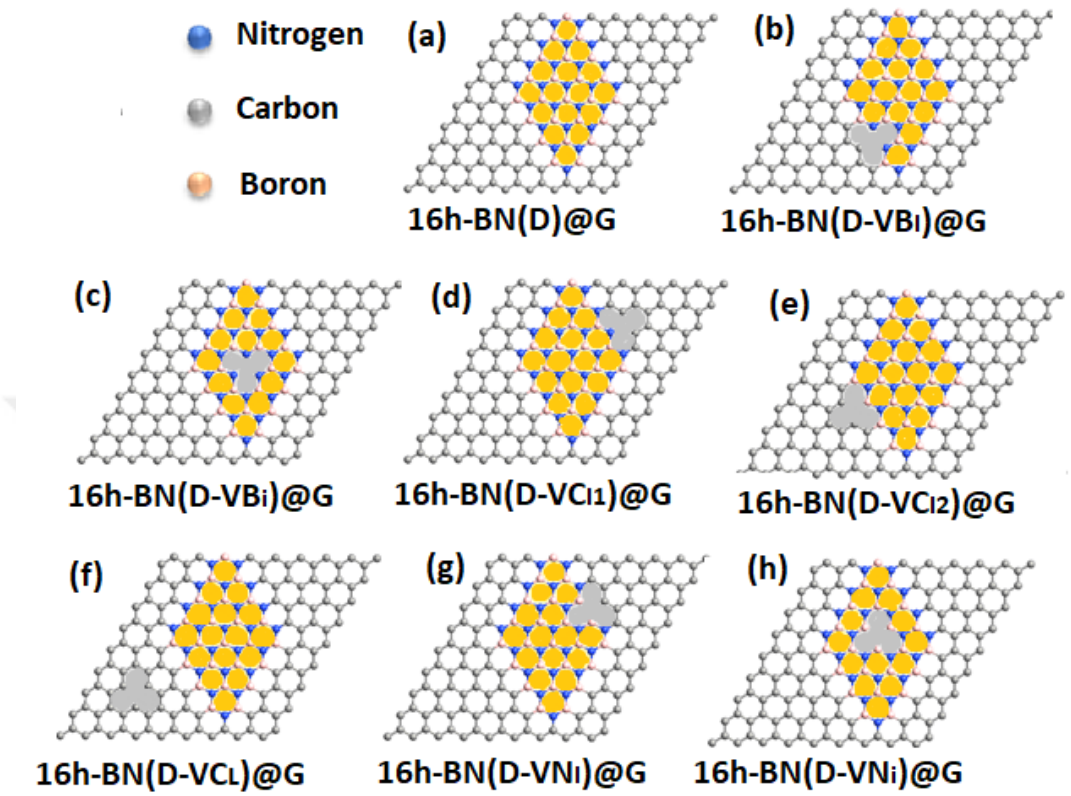

Figure 25 Optimized geometries of defect-free and defective GBN hybrids. The graphene layout hosts a diamond shaped h-BN island with size 16. The h-BN island was highlighted in yellow. The vacancy was highlighted in gray. The legend with color indication is shown at the top left corner.

3.3.2.2. Electronic band structure

The calculated band gap energies for the defect-free hybrids with h-BN islands were tabulated in **Table 1**. All defect-free hybrids display semiconducting features. The band gap of the defect-free hybrids increases with increasing h-BN island size. The energy band structures of various defective hybrids with h-BN islands were displayed in **Figure** 26. As can be seen in **Table 5**, the VC_{I1} defected hybrid with h-BN size 4, the VC_{I2} defected hybrid with h-BN size 9, and the VC_{L} defected hybrid with h-BN size 16 show semiconducting features. The remaining defective hybrids in **Table 5** show metallic features. As seen in **Figure 26**, non-flat energy bands exist near the Fermi level of defective hybrids.

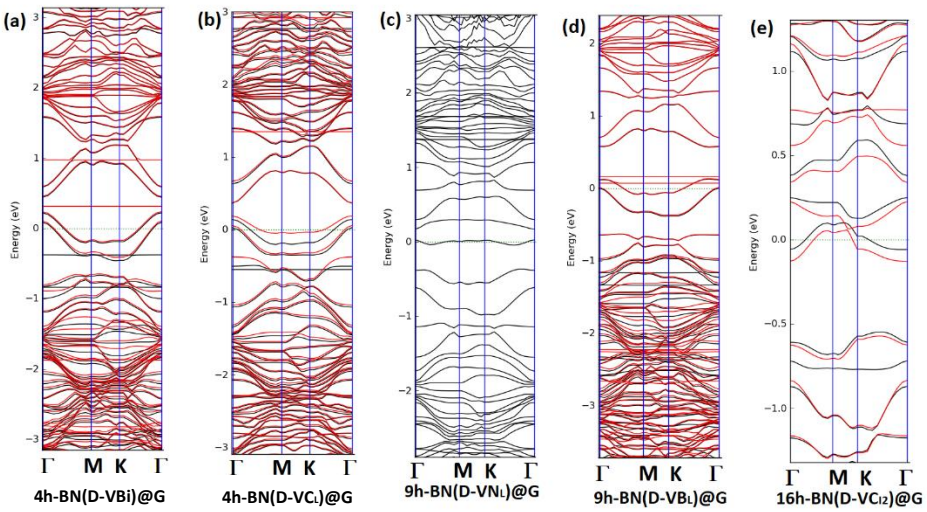

Figure 26 Electronic band structures of various defective hybrids shown in **Figure** 22 having unique structural and electronic properties. The energy bands of spin up (spin down) electrons are shown in red (black). The horizontal dotted line in green represents the Fermi level. Spin splitting can clearly be noticed except for 9h-BN(D-VN_L)@G.

A correlation could not be observed between the band gap of defective hybrid and the size of h-BN island. The energy band structures of hybrids which are not shown in **Figure 26** display similar non-flat bands near E_F . We showed their energy band structures in **Figure 27**, **Figure 28** and **Figure 29**.

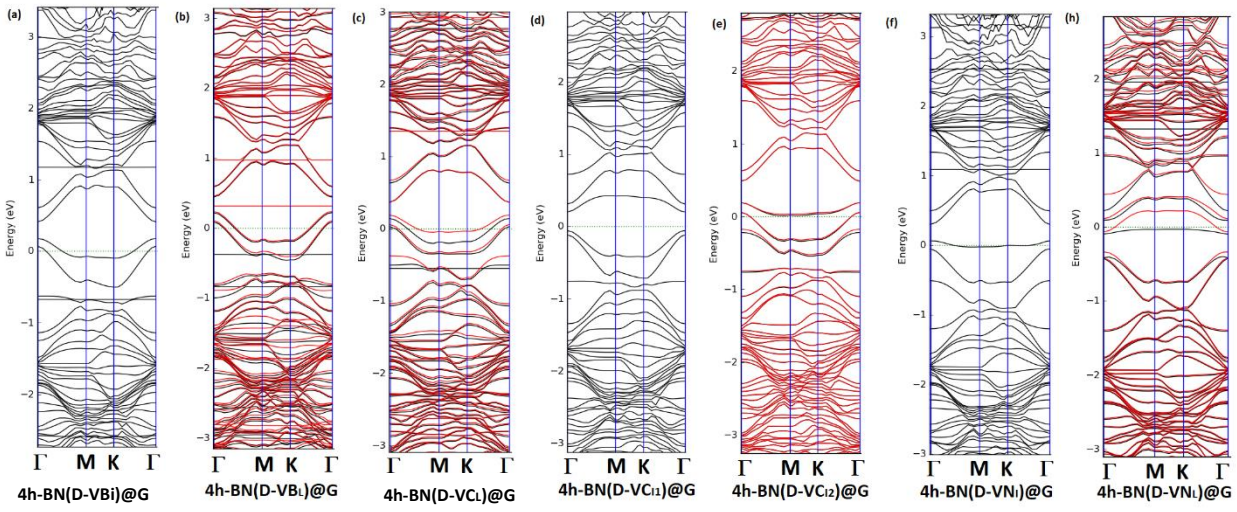

Figure 27 Electronic band structures of defective hybrids including h-BN islands with size 4. All defective hybrids show non-flat energy bands near the Fermi level.

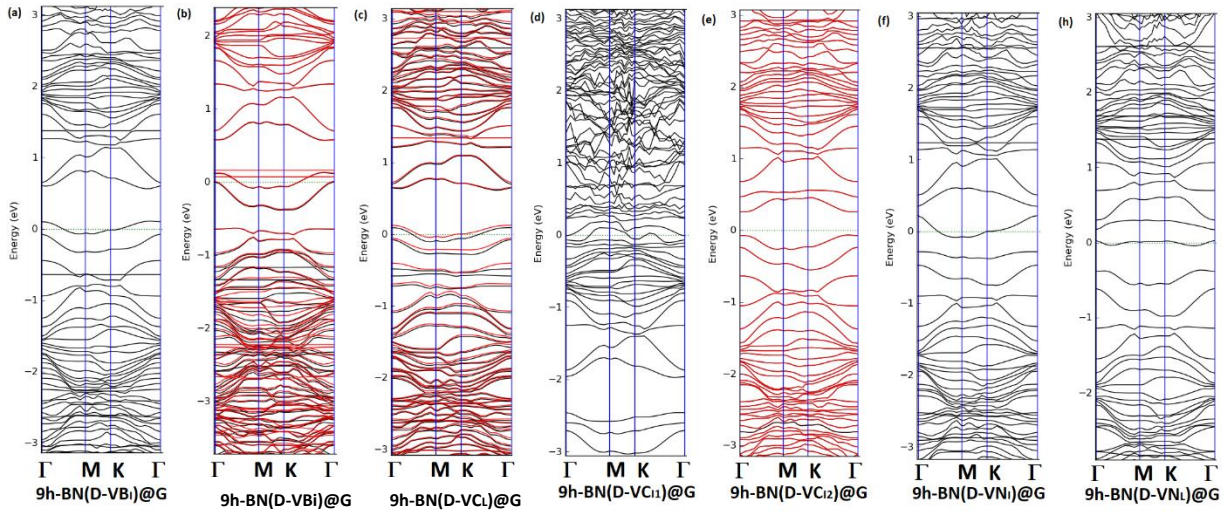

Figure 28 Electronic band structures of defective hybrids including h-BN islands with size 9. All defective hybrids show non-flat energy bands near the Fermi level.

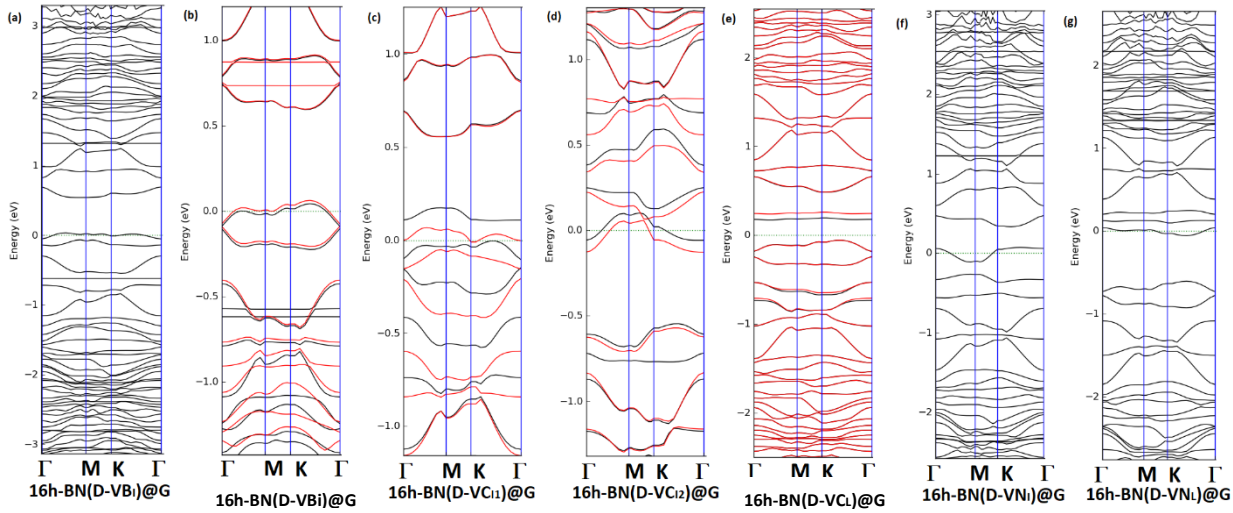

Figure 29 Electronic band structures of defective hybrids including h-BN islands with size 16. All defective hybrids show non-flat energy bands near the Fermi level except for the system given in (e).

4.0 CONCLUSION

The energetics of single vacancies and the impact they have on magnetic, structural and electronic, properties of in-plane GBN hybrid nanostructures were investigated by employing DFT computations. The defect-free GBN nanosheets are all non-magnetic and the band gap reduces with increasing size of G island for hybrids G(D)@h-BN. Besides, the band gap decreases with shrinking h-BN island in h-BN(D)@G hybrids.After optimizing the defect-free GBN hybrid, single vacancy was created by pulling out one either N, B or C atom at 7 distinct spots of the defect-free nanosheet to compute the material properties and defect formation energies of defective hybrids. With the change in the vacancy sites, the vacancy formation energy differs considerably. After the full optimizations of defective hybrids, structural reconstruction was not observed but there is a slight distortion in the vicinity of the vacancy. For G@h-BN hybrids, relationship between vacancy formation energy and island size could not be established. Because the C-N bond is possibly stronger than the C-B one, the C vacancy around the B atom has lower formation energy. The vacancy specifically at the G-BN interface presents lower defect formation energy.

Considering the results, it can be concluded that the most energetically favorable place for the creation of single vacancy is the interface. For G@h-BN systems, the single vacancy induces flat energy bands near the E_F. For G@h-BN hybrid with 4 hexagonal units, the VB_L defect exhibits a metallic property in its electronic band structure and shows a considerable amount of magnetic moment. The hybrids containing the graphene island in sizes 9 and 16 have the highest magnetization energy in VB_L defected system, while hybrids with G island size 4 has the highest magnetization energy on VB_I defected system.Similarly, for the island sizes 9 and 16, the GBN hybrid retains both a substantial amount of magnetic moment and magnetization energy when it involves the defect VB_L. In addition to this, the hybrid involving a G island with size 16 and VC_{I2} acquires a substantial amount of magnetic moment and magnetization energy. Hybrid that possesses a substantial amount of ΔE_M also has a band gap in the range of 0.02–1.1 eV. Based on our results, they could be potential candidates for spintronics and magnetic applications. For h-BN@G systems, the VC defects at the interface of hybrid were discovered to possess no magnetic moment as the h-BN island is in size 4. However, they acquire a small amount of magnetic moment as the h-BN island grows in size. All VN defected hybrids have a magnetic moment of 1 μ_B for the h-BN size 4. Likewise, the VN_i defect acquires a magnetic moment of 1 μ_B for the h-BN size 9. Remaining VN defected hybrids have no magnetic moments in our DFT calculations. The VB_i defected hybrid has the largest value of magnetic moment regardless of size of the h-BN island. The VB_L defected hybrids with G islands in sizes of 9 and 16 have the highest amount of magnetic moments. We could not obtain a correlation between the band gap of defective hybrid and the size of h-BN island embedded in G layout. The results of this research show that the band gap of h-BN nanosheet can be closed and tuned by implanting a suitable size of graphene island. Band gap opening in graphene nanosheet and band gap tuning in functionalized graphene nanosheet can also

be realized by implanting a suitable size of h-BN island. The magnetism of GBN hybrids can also be manipulated by means of vacancy defect.

5.0 REFERENCES

[1] K. S. Novoselov *et al.*, "Electric field in atomically thin carbon films," *Science (80-.).*, 2004, doi: 10.1126/science.1102896.

[2] D. A. Areshkin and C. T. White, "Building blocks for integrated graphene circuits," *Nano Lett.*, 2007, doi: 10.1021/nl070708c.

[3] R. M. Westervelt, "Applied physics: Graphene nanoelectronics," *Science*. 2008, doi: 10.1126/science.1156936.

[4] D. Long, W. Li, L. Ling, J. Miyawaki, I. Mochida, and S. H. Yoon, "Preparation of nitrogen-doped graphene sheets by a combined chemical and hydrothermal reduction of graphene oxide," *Langmuir*, 2010, doi: 10.1021/la102425a.

[5] G. Jo, M. Choe, S. Lee, W. Park, Y. H. Kahng, and T. Lee, "The application of graphene as electrodes in electrical and optical devices," *Nanotechnology*. 2012, doi: 10.1088/0957-4484/23/11/112001.

[6] S. Agnoli and M. Favaro, "Doping graphene with boron: A review of synthesis methods, physicochemical characterization, and emerging applications," *Journal of Materials Chemistry A*. 2016, doi: 10.1039/c5ta10599d.

[7] A. L. M. Reddy, A. Srivastava, S. R. Gowda, H. Gullapalli, M. Dubey, and P. M. Ajayan, "Synthesis of nitrogen-doped graphene films for lithium battery application," *ACS Nano*, 2010, doi: 10.1021/nn101926g.

[8] O. Ovdat, J. Mao, Y. Jiang, E. Y. Andrei, and E. Akkermans, "Observing a scale anomaly and a universal quantum phase transition in graphene," *Nat. Commun.*, 2017, doi: 10.1038/s41467-017-00591-8.

[9] Y. Zhang *et al.*, "Scanning tunneling microscopy of the π magnetism of a single carbon vacancy in graphene," *Phys. Rev. Lett.*, 2016, doi: 10.1103/PhysRevLett.117.166801.

[10] H. P. Boehm, A. Clauss, G. O. Fischer, and U. Hofmann, "Dünnste kohlenstoff-folien," *Zeitschrift fur Naturforsch. - Sect. B J. Chem. Sci.*, 1962, doi: 10.1515/znb-1962-0302.

[11] A. Hamwi, S. Mouras, D. Djurado, and J. C. Cousseins, "New synthesis of first stage graphite intercalation compounds with fluorides," *J. Fluor. Chem.*, 1987, doi: 10.1016/0022-1139(87)95120-7.

[12] P. L. De Andres, R. Ramírez, and J. A. Vergés, “Strong covalent bonding between two graphene layers,” *Phys. Rev. B - Condens. Matter Mater. Phys.*, 2008, doi: 10.1103/PhysRevB.77.045403.

[13] A. J. Van Bommel, J. E. Crombeen, and A. Van Tooren, “LEED and Auger electron observations of the SiC(0001) surface,” *Surf. Sci.*, 1975, doi: 10.1016/0039-6028(75)90419-7.

[14] D. V. Badami, “Graphitization of α-silicon carbide,” *Nature*, 1962, doi: 10.1038/193569a0.

[15] X. Li *et al.*, “Large-area synthesis of high-quality and uniform graphene films on copper foils,” *Science (80-.).*, 2009, doi: 10.1126/science.1171245.

[16] Z. Li *et al.*, “Field and temperature dependence of intrinsic diamagnetism in graphene: Theory and experiment,” *Phys. Rev. B - Condens. Matter Mater. Phys.*, 2015, doi: 10.1103/PhysRevB.91.094429.

[17] P. Puneet *et al.*, “Enhancement of thermoelectric performance of ball-milled bismuth due to spark-plasma-sintering-induced interface modifications,” *Adv. Mater.*, 2013, doi: 10.1002/adma.201204010.

[18] M. H. Gass, U. Bangert, A. L. Bleloch, P. Wang, R. R. Nair, and A. K. Geim, “Free-standing graphene at atomic resolution,” *Nat. Nanotechnol.*, 2008, doi: 10.1038/nnano.2008.280.

[19] J. C. Meyer, C. Kisielowski, R. Erni, M. D. Rossell, M. F. Crommie, and A. Zettl, “Direct imaging of lattice atoms and topological defects in graphene membranes,” *Nano Lett.*, 2008, doi: 10.1021/nl801386m.

[20] A. K. Geim and K. S. Novoselov, “The rise of graphene,” in *Nanoscience and Technology: A Collection of Reviews from Nature Journals*, 2009.

[21] S. Tang *et al.*, “Precisely aligned graphene grown on hexagonal boron nitride by catalyst free chemical vapor deposition,” *Sci. Rep.*, 2013, doi: 10.1038/srep02666.

[22] W. Yang *et al.*, “Epitaxial growth of single-domain graphene on hexagonal boron nitride,” *Nat. Mater.*, 2013, doi: 10.1038/nmat3695.

[23] Z. Liu *et al.*, “In-plane heterostructures of graphene and hexagonal boron nitride with controlled domain sizes,” *Nat. Nanotechnol.*, 2013, doi: 10.1038/nnano.2012.256.

[24] T. B. Martins, R. H. Miwa, A. J. R. Da Silva, and A. Fazzio, “Electronic and transport properties of boron-doped graphene nanoribbons,” *Phys. Rev. Lett.*, 2007, doi: 10.1103/PhysRevLett.98.196803.

[25] A. Quandt, C. Özdoğan, J. Kunstmann, and H. Fehske, “Boron doped graphene nanostructures,” in *Physica Status Solidi (B) Basic Research*, 2008, doi: 10.1002/pssb.200879559.

[26] T. Ohta, A. Bostwick, T. Seyller, K. Horn, and E. Rotenberg, “Controlling the electronic structure of bilayer graphene,” *Science (80-.).*, 2006, doi: 10.1126/science.1130681.

[27] Y. W. Son, M. L. Cohen, and S. G. Louie, “Energy gaps in graphene nanoribbons,” *Phys. Rev. Lett.*, 2006, doi: 10.1103/PhysRevLett.97.216803.

[28] D. J. Appelhans, Z. Lin, and M. T. Lusk, “Two-dimensional carbon semiconductor: Density functional theory calculations,” *Phys. Rev. B - Condens. Matter Mater. Phys.*, 2010, doi: 10.1103/PhysRevB.82.073410.

[29] S. Park and R. S. Ruoff, “Chemical methods for the production of graphenes,” *Nat. Nanotechnol.*, 2009, doi: 10.1038/nnano.2009.58.

[30] D. PaciÍ, J. C. Meyer, Ç. Girit, and A. Zettl, “The two-dimensional phase of boron nitride: Few-atomic-layer sheets and suspended membranes,” *Appl. Phys. Lett.*, 2008, doi: 10.1063/1.2903702.

[31] M. Engler and B. Ruisinger, “Hexagonal Boron Nitride (hBN) – Applications from Metallurgy to cosmetics,” *Ceram. forum Int.*, 2007.

[32] V. L. Solozhenko, A. G. Lazarenko, J. P. Petitet, and A. V. Kanaev, “Bandgap energy of graphite-like hexagonal boron nitride,” *J. Phys. Chem. Solids*, 2001, doi: 10.1016/S0022-3697(01)00030-0.

[33] A. Catellani, M. Posternak, A. Baldereschi, and A. J. Freeman, “Bulk and surface electronic structure of hexagonal boron nitride,” *Phys. Rev. B*, 1987, doi: 10.1103/PhysRevB.36.6105.

[34] K. Watanabe, T. Taniguchi, and H. Kanda, “Direct-bandgap properties and evidence for ultraviolet lasing of hexagonal boron nitride single crystal,” *Nat. Mater.*, 2004, doi: 10.1038/nmat1134.

[35] M. SokoŁowski, “Deposition of wurtzite type boron nitride layers by reactive pulse

plasma crystallization," *Journal of Crystal Growth*. 1979, doi: 10.1016/0022-0248(79)90121-0.

[36] L. Shen, B. J. Tan, W. S. Willis, F. S. Galasso, and S. L. Suib, "Characterization of Dip-Coated Boron Nitride on Silicon Carbide Fibers," *J. Am. Ceram. Soc.*, 1994, doi: 10.1111/j.1151-2916.1994.tb07260.x.

[37] C. Zhi, Y. Bando, C. Tang, H. Kuwahara, and D. Golberg, "Large-scale fabrication of boron nitride nanosheets and their utilization in polymeric composites with improved thermal and mechanical properties," *Adv. Mater.*, 2009, doi: 10.1002/adma.200900323.

[38] L. Song *et al.*, "Large scale growth and characterization of atomic hexagonal boron nitride layers," *Nano Lett.*, 2010, doi: 10.1021/nl1022139.

[39] A. Zunger and A. Katzir, "Point defects in hexagonal boron nitride. II. Theoretical studies," *Phys. Rev. B*, 1975, doi: 10.1103/PhysRevB.11.2378.

[40] S. Azevedo, J. R. Kaschny, C. M. C. De Castilho, and F. De Brito Mota, "A theoretical investigation of defects in a boron nitride monolayer," *Nanotechnology*, 2007, doi: 10.1088/0957-4484/18/49/495707.

[41] Y. Lin, T. V. Williams, W. Cao, H. E. Elsayed-Ali, and J. W. Connell, "Defect functionalization of hexagonal boron nitride nanosheets," *J. Phys. Chem. C*, 2010, doi: 10.1021/jp105454w.

[42] N. Alem *et al.*, "Probing the out-of-plane distortion of single point defects in atomically thin hexagonal boron nitride at the picometer scale," *Phys. Rev. Lett.*, 2011, doi: 10.1103/PhysRevLett.106.126102.

[43] A. Zobelli, C. P. Ewels, A. Gloter, and G. Seifert, "Vacancy migration in hexagonal boron nitride," *Phys. Rev. B - Condens. Matter Mater. Phys.*, 2007, doi: 10.1103/PhysRevB.75.094104.

[44] A. Y. Liu, R. M. Wentzcovitch, and M. L. Cohen, "Atomic arrangement and electronic structure of BC2N," *Phys. Rev. B*, 1989, doi: 10.1103/PhysRevB.39.1760.

[45] S. Azevedo and R. De Paiva, "Structural stability and electronic properties of carbon-boron nitride compounds," *Europhys. Lett.*, 2006, doi: 10.1209/epl/i2006-10066-0.

[46] K. Suenaga, C. Colliex, N. Demoncy, A. Loiseau, H. Pascard, and F. Willaime, "Synthesis of nanoparticles and nanotubes with well-separated layers of boron nitride and carbon,"

Science (80-.)., 1997, doi: 10.1126/science.278.5338.653.

[47] W.-Q. Han, W. Mickelson, J. Cumings, and A. Zettl, "Transformation of B/sub x/C/sub y/N/sub z/ nanotubes to pure BN nanotubes," *Applied Physics Letters*. 2002.

[48] C. Popov, K. Saito, B. Ivanov, Y. Koga, S. Fujiwara, and V. Shanov, "Chemical vapour deposition of BC2N films and their laser-induced etching with SF6," *Thin Solid Films*, 1998, doi: 10.1016/S0040-6090(97)00694-9.

[49] M. A. Mannan *et al.*, "Orientation of B-C-N hybrid films deposited on Ni (111) and polycrystalline Ti substrates explored by X-ray absorption spectroscopy," *Thin Solid Films*, 2011, doi: 10.1016/j.tsf.2010.09.052.

[50] A. Ramasubramaniam and D. Naveh, "Carrier-induced antiferromagnet of graphene islands embedded in hexagonal boron nitride," *Phys. Rev. B - Condens. Matter Mater. Phys.*, 2011, doi: 10.1103/PhysRevB.84.075405.

[51] Y. W. Son, M. L. Cohen, and S. G. Louie, "Half-metallic graphene nanoribbons," *Nature*, 2006, doi: 10.1038/nature05180.

[52] J. W. Jiang, J. S. Wang, and B. S. Wang, "Minimum thermal conductance in graphene and boron nitride superlattice," *Appl. Phys. Lett.*, 2011, doi: 10.1063/1.3619832.

[53] C. R. Dean *et al.*, "Boron nitride substrates for high-quality graphene electronics," *Nat. Nanotechnol.*, 2010, doi: 10.1038/nnano.2010.172.

[54] S. Bhowmick, A. K. Singh, and B. I. Yakobson, "Quantum dots and nanoroads of graphene embedded in hexagonal boron nitride," *J. Phys. Chem. C*, 2011, doi: 10.1021/jp200671p.

[55] N. Ding, X. Chen, and C. M. L. Wu, "Mechanical properties and failure behaviors of the interface of hybrid graphene/hexagonal boron nitride sheets," *Sci. Rep.*, 2016, doi: 10.1038/srep31499.

[56] Y. Fan *et al.*, "Manifold electronic structure transition of BNC biribbons," *J. Appl. Phys.*, 2011, doi: 10.1063/1.3619800.

[57] Y. Fan *et al.*, "Theoretical insights into the built-in electric field and band offsets of BN/C heterostructured zigzag nanotubes," *J. Phys. D. Appl. Phys.*, 2011, doi: 10.1088/0022-3727/44/9/095405.

[58] J. Nakamura, T. Nitta, and A. Natori, "Electronic and magnetic properties of BNC

ribbons," *Phys. Rev. B - Condens. Matter Mater. Phys.*, 2005, doi: 10.1103/PhysRevB.72.205429.

[59] R. M. dos Santos, R. B. Santos, B. G. E. Neto, G. M. e. Silva, and L. A. R. Junior, "Defective graphene domains in boron nitride sheets," *J. Mol. Model.*, 2019, doi: 10.1007/s00894-019-4093-5.

[60] N. Akman and C. Özdoğan, "Island shape, size and interface dependency on electronic and magnetic properties of graphene hexagonal-boron nitride (h-BN) in-plane hybrids," *J. Phys. Chem. Solids*, 2018, doi: 10.1016/j.jpcs.2017.12.025.

[61] K. Einalipour Eshkalak, S. Sadeghzadeh, and M. Jalaly, "The mechanical design of hybrid graphene/boron nitride nanotransistors: Geometry and interface effects," *Solid State Commun.*, 2018, doi: 10.1016/j.ssc.2017.12.001.

[62] G. Giovannetti, P. A. Khomyakov, G. Brocks, P. J. Kelly, and J. Van Den Brink, "Substrate-induced band gap in graphene on hexagonal boron nitride: Ab initio density functional calculations," *Phys. Rev. B - Condens. Matter Mater. Phys.*, 2007, doi: 10.1103/PhysRevB.76.073103.

[63] G. Lee, G. Yang, A. Cho, J. W. Han, and J. Kim, "Defect-engineered graphene chemical sensors with ultrahigh sensitivity," *Phys. Chem. Chem. Phys.*, 2016, doi: 10.1039/c5cp04422g.

[64] X. Wang *et al.*, "N-doping of graphene through electrothermal reactions with ammonia," *Science (80-.).*, 2009, doi: 10.1126/science.1170335.

[65] A. Hashimoto, K. Suenaga, A. Gloter, K. Urita, and S. Iijima, "Direct evidence for atomic defects in graphene layers," *Nature*, 2004, doi: 10.1038/nature02817.

[66] Z. H. Sheng, H. L. Gao, W. J. Bao, F. Bin Wang, and X. H. Xia, "Synthesis of boron doped graphene for oxygen reduction reaction in fuel cells," *J. Mater. Chem.*, 2012, doi: 10.1039/c1jm14694g.

[67] M. M. Ugeda, I. Brihuega, F. Guinea, and J. M. Gómez-Rodríguez, "Missing atom as a source of carbon magnetism," *Phys. Rev. Lett.*, 2010, doi: 10.1103/PhysRevLett.104.096804.

[68] G. Cassabois, P. Valvin, and B. Gil, "Hexagonal boron nitride is an indirect bandgap semiconductor," *Nat. Photonics*, 2016, doi: 10.1038/nphoton.2015.277.

[69] D. Nandwana and E. Ertekin, “Ripples, strain, and misfit dislocations: Structure of graphene-boron nitride superlattice interfaces,” *Nano Lett.*, 2015, doi: 10.1021/nl505005t.

[70] M. Li, B. Zheng, K. Duan, Y. Zhang, Z. Huang, and H. Zhou, “Effect of Defects on the Thermal Transport across the Graphene/Hexagonal Boron Nitride Interface,” *J. Phys. Chem. C*, 2018, doi: 10.1021/acs.jpcc.8b02750.

[71] P. Hohenberg and W. Kohn, “Inhomogeneous electron gas,” *Phys. Rev.*, 1964, doi: 10.1103/PhysRev.136.B864.

[72] W. Kohn and L. J. Sham, “Self-consistent equations including exchange and correlation effects,” *Phys. Rev.*, 1965, doi: 10.1103/PhysRev.140.A1133.

[73] K. Burke and L. O. Wagner, “DFT in a nutshell,” *International Journal of Quantum Chemistry*. 2013, doi: 10.1002/qua.24259.

[74] J. P. Perdew, A. Ruzsinszky, J. Tao, V. N. Staroverov, G. E. Scuseria, and G. I. Csonka, “Prescription for the design and selection of density functional approximations: More constraint satisfaction with fewer fits,” *J. Chem. Phys.*, 2005, doi: 10.1063/1.1904565.

[75] A. D. Becke, “Perspective: Fifty years of density-functional theory in chemical physics,” *J. Chem. Phys.*, 2014, doi: 10.1063/1.4869598.

[76] J. P. Perdew *et al.*, “Atoms, molecules, solids, and surfaces: Applications of the generalized gradient approximation for exchange and correlation,” *Phys. Rev. B*, 1992, doi: 10.1103/PhysRevB.46.6671.

[77] A. D. Becke, “Density-functional exchange-energy approximation with correct asymptotic behavior,” *Phys. Rev. A*, 1988, doi: 10.1103/PhysRevA.38.3098.

[78] C. D. Sherrill, “Frontiers in electronic structure theory,” *J. Chem. Phys.*, 2010, doi: 10.1063/1.3369628.

[79] I. J. Casely, J. W. Ziller, M. Fang, F. Furche, and W. J. Evans, “Facile bismuth-oxygen bond cleavage, C-H activation, and formation of a monodentate carbon-bound oxyaryl dianion, (C6H2tBu2-3,5-O-4)2-,” *J. Am. Chem. Soc.*, 2011, doi: 10.1021/ja201128d.

[80] J. P. Perdew and Y. Wang, “Accurate and simple analytic representation of the electron-gas correlation energy,” *Phys. Rev. B*, 1992, doi: 10.1103/PhysRevB.45.13244.

[81] G. Kresse and J. Furthmüller, “Efficiency of ab-initio total energy calculations for metals and semiconductors using a plane-wave basis set,” *Comput. Mater. Sci.*, 1996, doi:

10.1016/0927-0256(96)00008-0.

[82] G. Kresse and J. Furthmüller, “Efficient iterative schemes for ab initio total-energy calculations using a plane-wave basis set,” *Phys. Rev. B - Condens. Matter Mater. Phys.*, 1996, doi: 10.1103/PhysRevB.54.11169.

[83] P. E. Blöchl, O. Jepsen, and O. K. Andersen, “Improved tetrahedron method for Brillouin-zone integrations,” *Phys. Rev. B*, 1994, doi: 10.1103/PhysRevB.49.16223.

[84] G. Kresse and D. Joubert, “Kresse, Joubert - Unknown - From ultrasoft pseudopotentials to the projector augmented-wave method,” *Phys. Rev. B*, 1999.

[85] M. Methfessel and A. T. Paxton, “High-precision sampling for Brillouin-zone integration in metals,” *Phys. Rev. B*, 1989, doi: 10.1103/PhysRevB.40.3616.

[86] H. A. Hussain, N. Akman, and C. Özdoğan, “Investigation of the mono vacancy effects on the structural, electronic and magnetic properties of graphene hexagonal-boron nitride in-plane hybrid embracing diamond shaped graphene island,” *Solid State Sci.*, 2020, doi: 10.1016/j.solidstatesciences.2020.106395.

[87] M. Kolos and F. Karlický, “Accurate many-body calculation of electronic and optical band gap of bulk hexagonal boron nitride,” *Phys. Chem. Chem. Phys.*, 2019, doi: 10.1039/c8cp07328g.

[88] Y. Shi *et al.*, “Synthesis of few-layer hexagonal boron nitride thin film by chemical vapor deposition,” *Nano Lett.*, 2010, doi: 10.1021/nl1023707.

[89] C. Elias *et al.*, “Direct band-gap crossover in epitaxial monolayer boron nitride,” *Nat. Commun.*, 2019, doi: 10.1038/s41467-019-10610-5.

[90] N. Akman and C. Özdoğan, “Vacancy induced robust magnetism in graphene hexagonal-boron nitride in-plane hybrids with hexagonal shaped islands,” *J. Magn. Magn. Mater.*, 2020, doi: 10.1016/j.jmmm.2020.166530.

[91] R. W. G. Wyckoff, “Crystal structure of uraninite,” in *Crystal Structures 1*, 1963.

[92] C. Ö. Zdoğan, S. Mukhopadhyay, W. Hayami, Z. B. Güvenc, R. Pandey, and S. Boustani, “The unusually stable B100 Fullerene, structural transitions in boron nanostructures, and a comparative study of α- and γ-boron and sheets,” *J. Phys. Chem. C*, 2010, doi: 10.1021/jp911641u.

[93] R. R. Nair *et al.*, “Spin-half paramagnetism in graphene induced by point defects,” *Nat. Phys.*, 2012, doi: 10.1038/nphys2183.

6.0 APPENDIX

6.1 VASP INPUT files

To explain the input and output files used by VASP we will consider running a calculation for unit cell of h-BN. First to relax the structure to its ground state. The most important files are POSCAR, INCAR, , KPOINTS, POTCAR

- **INCAR file**

  This is the primary input file in VASP. The file contains the instruction of what to do and how to do it, can consist of fairly huge number of parameters. The parameters are mostly default. User should not change these default values, if not familiar with them

Below are some of the INCAR file tags, many more tags can be set

```
ENCUT = 400
NSW = 300
EDIFF = 1E-5
EDIFFG = 0.001
ISIF = 3
IBRION = 2
```

- **ENCUT tag:** Set the energy cutoff for plan wave basis set in eV, it needs to be tested by convergence testing.
- **NSW tag:** Sets the maximum electronic steps. To prevent a nonconverging calculation to run forever.
- **EDIFF tag:** Sets the global break condition for electrons in the SI-loop.

- **IBRION ta**g: Decides how ions are updated and moved. Numbers 0,1,2 correspond to different algorism.

➢ **POSCAR file**

Contains the coordinates use to create the virtual representation of the structure, it contains ionic positions and lattice geometry.

```
B N
0.940000000000
        1.251995000000      -2.168518950822      0.000000000000
        1.251995000000       2.168518950822      0.000000000000
        0.000000000000       0.000000000000      6.661200000000
B       N
2       2
Direct
        0.333333333333       0.666666666667      0.250000000000
        0.666666666667       0.333333333333      0.750000000000
        0.333333333333       0.666666666667      0.750000000000
        0.666666666667       0.333333333333      0.250000000000
```

➢ **POTCAR file**

POTCAR is one of the input file in VASP calculation it contain the pseudopotential information for each atomic particle used in the computation. For VASP to recognize which atoms are in the POSCAR file, one need to create a POTCAR file. The POTCAR file holds the pseudopotentials for all the different atoms. A pseudopotential is a modified expression for the potential that makes it possible to solve the Schrödinger equation. POTCAR file is relatively a huge file, the format of the file is shown below.

```
PAW-PBE B 07Oct2001
2.00000000000
parameter frm PSCT :
        VRHFI = B: s2p1
        LEXCH       = PE
        EATOM       = 61.203 eV,  5.331y


        LULTRA      = F use Utr_asofts PP ?
        RPACOR      = 1.200         core R
        ENMAX       = 318.61; E_MIN       = 238.960 eV
        RCORE       = 1.700         outer cut-off R
        LCOR        = T      charges
        IUNSCR      = 2      unscrn: 0-ln 1-nonln 2
        TITEL       = PAW_PBE B 06Sep2000
        POMASS      = 20.811; ZVA         = 3.00 M and V
        RWIGS       = 1.710; RWIG         = 0.905 W-seitz radius (A)
        ICORE       = 2      L potentials
        LPAW        = T      PP
        EAUG        = 535.514
        DEXC        = 0.000
        RMAX        = 1.732 core radius for proj-oper
```

The KPOINTS file is used to define the Bloch vectors (k-points) that will be applied in sampling the Brillouin zone in the calculation. There are several ways one may define the k-points in the KPOINTS file: (i) as an automatically generated (shifted) regular mesh of points, (ii) by means of the beginning and end-points of line segments, or (iii) as an explicit list of points and weights.

```
Automatic mesh      comment
0                   0= Automatic generation of k-points
Gamma               Generated Gamma centered k-mesh
24 24 1             Grid 24x24x1
```

6.2 OUTPUT FILES

- **CONTCAR file**

Contains position of the system after the calculation has completed.

The last ionic step during relaxation has its positions stored in CONTCAR file. Before continuing the calculation CONTCAR file is usually copied as POSCAR if the relaxation stage did not converge. POSCAR and CONTCAR file are identical in static calculations

- **OSZICAR file**

Contains data of electronic steps and ionic steps. Data about the current step and convergence speed is stored to OSZICAR.

- **OUTCAR file:**

All the information needed regarding the output of VASP calculation is found in OUTCAR file, this includes: Data on the electronic steps, information about input parameters, , KS-eigenvalues, stress tensors, forces on the atoms and so on.

- **CHGCAR file**

The file comprises of atomic coordinates, lattice vectors, PAW one-center occupancies and charge density. CHGCAR contains the code can be use to start the calculation all over again from the existing charge density